MODELING OF TRANSPORT AND TRANSFORMATION PROCESSES IN POROUS AND MULTIPHASE BODIES

Juraj Kosek[1], František Štěpánek[2] and Miloš Marek[1,*]

[1]**Department of Chemical Engineering, Prague Institute of Chemical Technology, Czech Republic**

[2]**Department of Chemical Engineering, Imperial College London, UK**

Abstract

A methodology for computer representation of the structure of spatially complex multiphase media and for the modeling of reaction, transport, and structure-transformation processes in those media, is reviewed.

*Tel.: +420 220 443 104; Fax: +420 233 337 335; E-mail: milos.marek@vscht.cz

Advances in Chemical Engineering, vol. 30
ISSN 0065 2377
DOI 10.1016/S0065-2377(05)30003-2

The methodology is demonstrated via several examples including phase transition and structure evolution in porous and granular media, the morphogenesis of polymer particles, and heterogeneous catalysis. Several future potential applications of the methodology are identified.

I. Introduction

Chemical engineering has always been concerned with describing phenomena occurring over a range of length-scales, from the molecular (e.g., adsorption equilibrium and reaction kinetics), through the mesoscopic (e.g., agglomeration), to continuum description of transport phenomena (e.g., momentum, heat, and mass transfer), up to the unit operation and process-systems levels. It has also been the aim to pass information from models at one length-scale to those at a different hierarchical level. For example, a fixed-bed catalytic reactor model may require the effectiveness factor as one of its input parameters, which can be obtained as a solution of a diffusion problem at the length-scale of an individual catalyst pellet (Sahimi *et al.*, 1990). The values of a diffusion coefficient or adsorption equilibrium constant (Davies and Seaton, 2000), which are required as input to the particle-scale model can, in turn, be obtained from molecular-level simulations.

Several length-scales have to be considered in a number of applications. For example, in a typical monolith reactor used as automobile exhaust catalytic converter the reactor length and diameter are on the order of decimeters, the monolith channel dimension is on the order of 1 mm, the thickness of the catalytic washcoat layer is on the order of tens of micrometers, the dimension of the pores in the washcoat is on the order of 1 μm, the diameter of active noble metal catalyst particles can be on the order of nanometers, and the reacting molecules are on the order of ångstroms; cf. Fig. 1. The modeling of such reactors is a typical multiscale problem (Hoebink and Marin, 1998). Electron microscopy accompanied by other techniques can provide information on particle size, shape, and chemical composition. Local composition and particle size of dispersed nanoparticles in the porous structure of the catalyst affect catalytic activity and selectivity (Bell, 2003).

Simulation techniques suitable for the description of phenomena at each length-scale are now relatively well established: Monte Carlo (MC) and Molecular Dynamics (MD) methods at the molecular length-scale, various ''mesoscopic'' simulation methods such as Dissipative Particle Dynamics (Groot and Warren, 1997), Brownian Dynamics, or Lattice Boltzmann in the colloidal domain, Computational Fluid Dynamics at the continuum length-scale, and sequential-modular or equation-based methods at the unit operation/process-systems level.

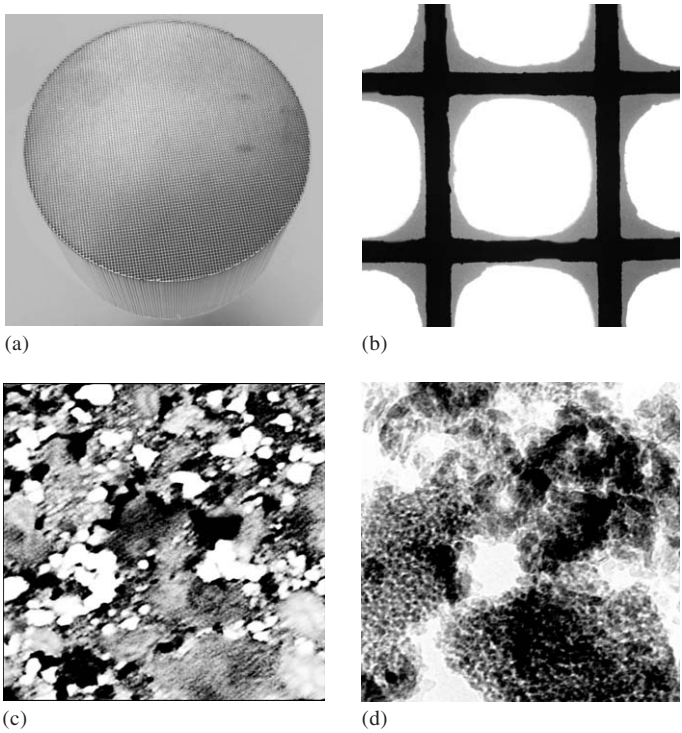

FIG. 1. The multiple scales in the catalytic monolith reactor: (a) catalytic monolith (10 cm), (b) channel with catalyst washcoat on the walls (1 mm), (c) SEM image of the washcoat layer (10 μm), (d) TEM image of meso-porous γ-Al_2O_3 with dispersed Pt (200 nm).

If in all situations, parameters could be transferred from models at one hierarchical level to another in the form of precalculated coefficients or closed-form expressions, such as an equation of state or a correlation for a mass-transfer coefficient, there would be no need for "multiscale modeling" as a distinct methodology. However, there are many situations where phenomena occurring at different length-scales are so integrated that their modeling cannot be simply de-coupled (Ingram *et al.*, 2004). As an example, one can consider gas-phase catalytic polymerization of olefins, where the resulting polymer properties (chain-length distribution, crystallinity) depend simultaneously on phenomena at several length-scales: from polymer growth around a catalyst-support fragment, through monomer diffusion and heat transfer within a growing polymer particle, to population dynamics and fluid-particle flow at the length-scale of the reactor (Kosek *et al.*, 2001a, b).

As the focus of chemical engineering research shifts from bulk and petrochemicals to specialty materials and formulated products, "microstructure" is becoming an increasingly important product attribute controlling end-use

properties. By microstructure we mean the spatial distribution of components, or phases, in the product. The distribution of amorphous and crystalline domains within a polymer particle, for example, has a significant influence on its further processability. The distribution of primary solid particles, binder, and porosity within a granule has an influence on its dissolution and release characteristics (Stepanek, 2004) and can control attributes such as the bioavailability of a drug.

In this chapter, we review modeling methods specifically aimed at describing transport and reaction phenomena that occur within, or lead to the formation of, complex porous or multiphase microstructures. The chapter is structured as follows. First, the methodology of computer representation, characterization, and reconstruction of multiphase and porous media is described. Techniques for computational determination of effective transport properties in digitally reconstructed media are then described, as well as methods for the modeling of transient transport/transformation processes in those media. The methods are then illustrated by selected examples from areas of interest of the authors: polymer particle morphogenesis, granule formation and dissolution, and heterogeneous catalysis. Other emerging applications are then mentioned in Section V, followed by concluding remarks in Section VI. Finally, a list of key literature references is provided.

II. Methodology

A. Representation of Multiphase Media

The structure of a multiphase medium can be specified by the spatial distribution of the phases that form the medium. This spatial distribution can be generally represented by the phase function or, in specific situations, by the equivalent pore-network diagram, by the spatial distribution of particles or other constituents, and by the probability density function. Examples of the representation of the porous media are shown in Fig. 2.

In the general case, the spatial distribution of the phases can be formally represented by the so-called *phase function* $f_i : \mathbb{R}^3 \rightarrow \{0; 1\}$ for each phase i. The phase function is defined as (Adler, 1992, 1994)

$$f_i(\boldsymbol{r}) = \begin{cases} 1 & \text{if } \boldsymbol{r} \in \text{phase } i \\ 0 & \text{otherwise} \end{cases} \tag{1}$$

By definition only one phase can be present at any point $\boldsymbol{r} \in \mathbb{R}^3$. It is further required that the set $\boldsymbol{P}_i \subset \mathbb{R}^3$, $\boldsymbol{P}_i = \{\boldsymbol{r} : f_i(\boldsymbol{r}) = 1\}$ be a compact set, i.e., that the inter-phase boundaries are smooth in the mathematical sense. In a discrete form, the phase function f_i becomes the phase volume function $\hat{f}_i$, which assigns

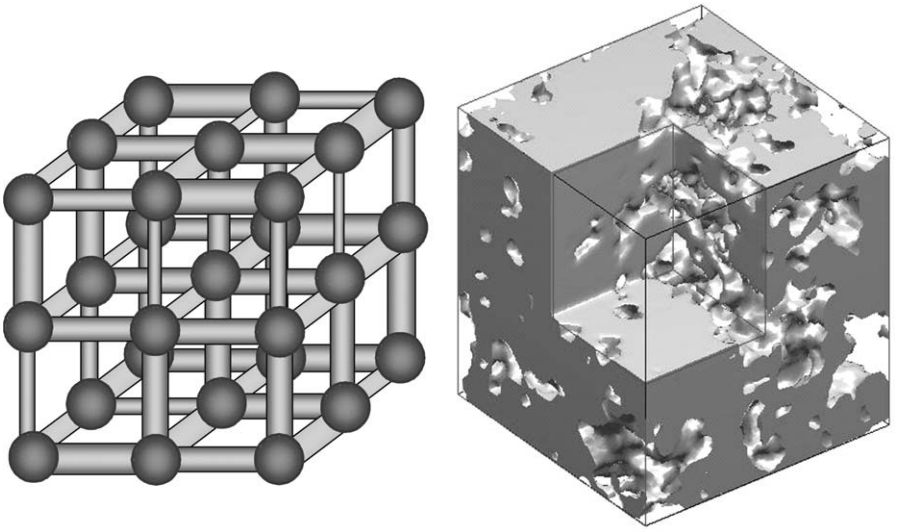

FIG. 2. Types of computer representation of porous media—network diagrams (left) and solid-phase function of reconstructed porous media (right).

each finite volume element of space (voxel) a value from the interval $\langle 0; 1 \rangle$, i.e., the volume fraction of phase i in that element. The sum of phase volume functions in each voxel must give unity,

$$\sum_i \hat{f}_i = 1 \tag{2}$$

and so for an N-phase medium only $N-1$ phase volume functions need to be specified in each voxel. Unless stated otherwise, we will further work only with phase volume functions on a discrete grid of voxels and leave out the hat notation from $\hat{f}_i$.

In a practical implementation, the domain on which the phase volume functions are specified is typically a cubic grid of $N_x \times N_y \times N_z$ voxels, which corresponds to real dimensions of $L_x = hN_x$, $L_y = hN_y$, and $L_z = hN_z$, where h is the voxel size. We will further call this region of real space the computational *unit cell*. The relationship between the unit cell and the multiphase medium of interest depends on the absolute dimensions of the medium and on the spatial resolution at which the medium is represented (feature dimensions). The unit cell can either contain the entire medium and some void space surrounding it, as in the case of virtual granules described in Section IV.D below, or be a sample of a much larger (theoretically infinite) medium, as in the case of transport properties calculation, described in Section II.E below.

In the latter case, the dimensions of the unit cell must be such that the unit cell is statistically representative of the entire medium. For spatially periodic regular media, the unit cell will coincide with one lattice unit. For random media, let $L_{\mathrm{m}} = \max_i(L_i)$ be the maximum characteristic length-scale of all the phases forming the medium, where L_i is defined by Eq. (4) below. The unit cell dimensions (L_x, L_y, L_z) should be much larger than the maximum characteristic length-scale L_{m} for transport properties calculated on the unit cell to become cell size-independent, and thus, representative of the entire medium (Adler, 1992).

In situations where the spatial features of the medium occur over a wide range of length-scales, e.g., in porous media with bi-modal pore size distribution (Salejova *et al.*, 2004), the voxel size h would have to be small enough to capture the smallest spatial feature but at the same time the unit cell size must be large enough for the sample to be statistically representative. This would require an infeasibly large number of voxels if standard fixed-grid encoding was used. In that case, one can use a spatially adaptive mesh (Perré, 2004; Sahimi *et al.*, 2004; Sapoval, 2001), or transform the porous medium into an equivalent pore-network model (Blunt *et al.*, 2002; El-Nafaty and Mann, 2001; Liang *et al.*, 2000a; Lin and Miller, 2000; Thompson, 2002).

As already mentioned, the phase function is only one of several possible ways of representing the structure of porous/multiphase media. Other alternatives include: (i) pore-network diagrams, (ii) density probability functions, and (iii) aggregate of interacting micro-elements. The mapping between those different types of spatially three dimensional (3D) representations is often required. However, the original structural data will nowadays almost always be in the form of a 2D or 3D digital image; therefore, their translation into a phase function is trivial as it involves just a spatial discretization. Some relevant structure acquisition techniques are now briefly reviewed.

B. Structure Acquisition

Information about the spatial distribution of phases in a specimen of a multiphase medium can be obtained experimentally by means of one of several techniques. Optical or scanning electron microscopy (SEM) yields spatially 2D images of surfaces or cross-sections of the material of interest. Modern electron microscopes provide resolution down to the atomistic level (e.g., Arenas-Alatorre *et al.*, 2002). When information about the chemical composition of a multiphase medium is required, spectroscopic imaging techniques such as IR imaging (Gupper *et al.*, 2002), energy dispersive X-ray (EDX) analysis, and X-ray photoelectron spectroscopy (XPS) can be used. Atomic force microscopy (AFM) can also be used for probing the microstructure of materials, e.g., the crystallinity in polymers (Hosier *et al.*, 2004) as well as a range of surface features. In the case of optical microscopy, standard staining can be used to

further distinguish between phases, as is commonly done when imaging biological tissue samples (Mantalaris *et al.*, 2001).

While standard optical and electron microscopy is limited to 2D imaging, confocal laser scanning microscopy (CLSM) can be used to probe the material to a certain depth and thus generate 3D information about its microstructure (Kanamori *et al.*, 2004). Several techniques can generate fully 3D images of porous or multiphase media. These include nuclear magnetic resonance (NMR) imaging (Barrie, 2000; Rigby and Daut, 2002), and tomographic reconstruction based on X-ray (Blacher *et al.*, 2004) or transmission electron microscopy (TEM) visualization (Weyland *et al.*, 2001). X-ray computed micro-tomography, in particular, has gained in popularity recently, being used for non-destructive 3D visualization of the microstructure of porous materials such as solid foams (Elmoutaouakkil *et al.*, 2002), textile (Ramaswamy *et al.*, 2004), or pharmaceutical granules (Farber *et al.*, 2003), as well as a range of biological materials. 3D TEM has been used for the direct visualization of metal nanocrystallites (Ichikawa *et al.*, 2003) and the pore structure of zeolites (Janssen *et al.*, 2001).

Once a spatially 2D or 3D image of the multiphase medium of interest has been obtained, it is desirable to characterize the image by a set of morphological descriptors, which can then be correlated with effective properties of the medium or their evolution followed in time when a structure-transformation process (e.g., dissolution) takes place in the medium. Let us now review some morphological descriptors most commonly used for the characterization of porous and multiphase media.

C. Morphological Characterization

The composition of the medium is expressed by the phase volume fraction ϕ_i of each phase i, which can be calculated as the spatial average (denoted by an overline) of its phase function f_i according to

$$\phi_i = \overline{f_i(\boldsymbol{r})} = \frac{1}{V}\int_V f_i(\boldsymbol{r})\,\mathrm{d}V \tag{3}$$

where $V = L_x L_y L_z$ is the volume of the unit cell. Specifically, porosity $\varepsilon = \phi_g$ is the volume fraction of the gas phase in an unsaturated porous medium. The next quantity of interest is the characteristic length-scale of each phase, which is a measure of its dispersion in the multiphase medium. Assuming non-fractal media, let S_i be the internal surface area of phase i (i.e., the area of its interface with all other phases). A characteristic length-scale L_i can be defined as

$$L_i = \frac{V_i}{S_i} = \frac{\phi_i V}{S_i} \tag{4}$$

Of particular interest in porous media is the so-called equivalent hydraulic diameter $d_e \equiv 4V_g/S_g = 4L_g$, which is important for permeability scaling (Martys and Garboczi, 1992).

In spatially evolving multiphase media (e.g., during dissolution of a porous medium, or phase separation in a polymer blend), the mean curvature of the interface between two phases is of interest. Curvature is a sensitive indicator of morphological transitions such as the transition from spherical to rod-like micelles in an emulsion, or the degree of sintering in a porous ceramic material. Furthermore, important physicochemical parameters such as capillary pressure (from the Young–Laplace equation) are curvature-dependent. The local value of the mean curvature $K_i = \frac{1}{2}(1/R_1 + 1/R_2)$ of an interface of phase i with principal radii of curvature R_1 and R_2 can be calculated as the divergence of the interface normal vector $\boldsymbol{n}_i$

$$K_i = -\nabla \cdot \boldsymbol{n}_i \tag{5}$$

where $\boldsymbol{n}_i$ is calculated as the gradient of the phase function

$$\boldsymbol{n}_i = -\frac{\nabla f_i}{||\nabla f_i||} \tag{6}$$

with the minus sign indicating normal vector orientation from the phase i to the surrounding phases. Higher-order approximations should be used for numerical evaluation of the gradient ∇f_i (Kothe *et al.*, 1996; Rider and Kothe, 1998; Scardovelli and Zaleski, 1999). The mean value of K_i is then obtained by averaging over the entire surface ∂_i of the phase i,

$$\overline{K_i} = \frac{1}{S_i}\int_{\partial_i} K_i \, \mathrm{d}A \tag{7}$$

The above-mentioned phase volume fractions, internal surface area, and mean curvature are instances of a more general class of integral measures called Minkowski functionals (Arns *et al.*, 2001, 2004).

Another frequently used characteristic of random media is the two-point autocorrelation function (Adler, 1992, 1994; Thovert *et al.*, 1993)

$$R_i(\boldsymbol{u}) = \frac{\overline{(f_i(\boldsymbol{r}) - \phi_i)(f_i(\boldsymbol{r}+\boldsymbol{u}) - \phi_i)}}{\overline{(f_i(\boldsymbol{r}) - \phi_i)^2}} \tag{8}$$

where ϕ_i is the phase volume fraction, and the overline denotes spatial average as defined by Eq. (3). In isotropic media, the correlation function does not depend on the direction, but only on the magnitude $u = ||\boldsymbol{u}||$ of the displacement vector. The zeroth moment of the correlation function,

$$L_{c,i} = \int_{u=0}^{\infty} R_i(u) \, \mathrm{d}u \tag{9}$$

is the so-called correlation length, an alternative measure of the characteristic length-scale of each phase in the multiphase medium. The characteristic length-scale of a phase in the medium can also be measured by the so-called chord-length distribution function (e.g., Roberts and Torquato, 1999), defined as the distribution of line segments passing through a given phase when the medium is randomly sampled by lines. The measure of characteristic length-scales is important from the physicochemical point of view, e.g., for measuring the mean pore diameter, which influences phenomena such as capillary condensation or Knudsen diffusivity.

In the context of diffusion in porous media, the tortuosity parameter τ has traditionally been used. Tortuosity is defined geometrically as the ratio of the shortest distance through the pore space between two randomly positioned points to their Euclidean distance, averaged over a large number of points. Tortuosity of the pore space (or any other percolating phase in a multiphase medium) can be evaluated directly from its phase function. The pore space distance of two points can be calculated using an algorithm based on the propagation of a reaction–diffusion front through the medium (Stepanek *et al.*, 2000). Topological properties of a percolating phase can further be characterized by reducing the phase into a skeleton (Liang *et al.*, 2000a) by applying a thinning algorithm. Skeletonization is useful for establishing the pore connectivity, or for distinguishing between the conducting and the dead-end pores in a porous medium.

Experimental techniques commonly used to measure pore size distribution, such as mercury porosimetry or BET analysis (Gregg and Sing, 1982), yield pore size distribution data that are not uniquely related to the pore space morphology. They are generated by interpreting mercury intrusion–extrusion or sorption hysteresis curves on the basis of an equivalent cylindrical pore assumption. To make direct comparison with digitally reconstructed porous media possible, morphology characterization methods based on simulated mercury porosimetry or simulated capillary condensation (Stepanek *et al.*, 1999) should be used.

D. Digital Reconstruction of Multiphase Media

The reconstruction of the porous/multiphase medium is the process starting from electron microscopy or other image of the medium, followed by the evaluation of suitable morphological descriptors of the image, concluding with the generation of a spatially 3D porous/multiphase medium with the same morphological characteristics as those of the original image. The reconstructed porous/multiphase medium is then used as the input for the calculation of effective transport, mechanical or electrical properties of the medium (Torquato, 2002), or as the input to the modeling of various reactions and other transformation processes.

In mathematical terms, given the porosity and suitable morphological characteristics, we want to construct the replica of the porous/multiphase medium

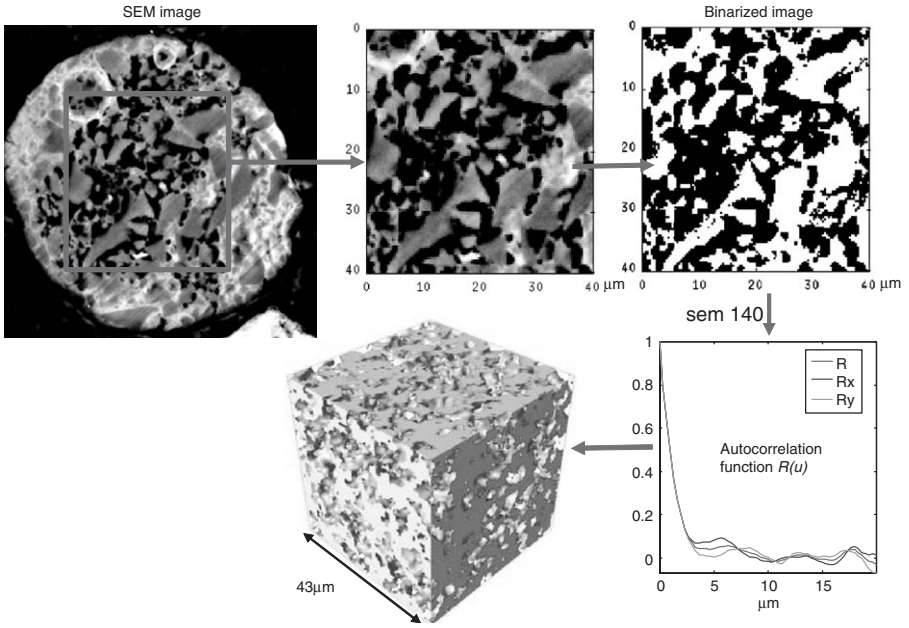

FIG. 3. Procedure of the reconstruction of porous media: SEM image of the porous silica-supported catalyst particle, selection of rectangular box, binarization of SEM image, calculation of the autocorrelation function $R(u)$, and reconstructed porous medium.

represented by the phase function $f_i(\boldsymbol{r})$ defined on the discrete grid of voxels with coordinates $\boldsymbol{r}$; cf. Fig. 3. Here, we present the principles of three different algorithms of the stochastic reconstruction of the porous/multiphase media: (i) simulated annealing, (ii) Poissonian generation of polydisperse spheres, and (iii) thresholding of correlated random fields. Then we briefly survey the reconstruction of porous media by mechanical diagenesis.

1. Simulated Annealing

Stochastic reconstruction by the simulated annealing algorithm is one of the most versatile classes of reconstruction methods, although not very efficient in terms of the computational demand. The increasing popularity of the simulated annealing algorithm (Hazlett, 1997; Manwart *et al.*, 2000) has been caused by ever-growing computational power and straightforward implementation.

Let us consider an isotropic porous medium under the reconstruction described by a pore phase function $f_g^{(k)}(\boldsymbol{r})$ in the kth iteration step of the simulated annealing algorithm and let the actual statistical characteristics of this phase function, i.e., the two-point correlation function, be $R_g^{(k)}(u)$. The distance of $R_g^{(k)}(u)$ from the target morphological characteristics $R_g^{\text{target}}(u)$ of the

microscopy image of the porous medium is

$$E_g^{(k)} = \sum_{u=0}^{u_{\max}} (R_g^{(k)}(u) - R_g^{\text{target}}(u))^2 \tag{10}$$

The simulated annealing algorithm typically starts from the random phase function $f_g^{(0)}(\boldsymbol{r})$ having the required porosity $\varepsilon = f_g^{(0)}(\boldsymbol{r})$. In the kth iteration step, we interchange the values of two voxels $f_g^{(k)}(\boldsymbol{r}_1)$ and $f_g^{(k)}(\boldsymbol{r}_2)$ at randomly chosen positions $\boldsymbol{r}_1$ and $\boldsymbol{r}_2$, where one voxel is from the pore and the other is from the solid phase, i.e., $f_g^{(k)}(\boldsymbol{r}_1) + f_g^{(k)}(\boldsymbol{r}_2) = 1$. Thus, a new phase configuration $f_g^{(k+1)}(\boldsymbol{r})$ is proposed and its statistical characteristics $R_g^{(k+1)}(u)$ as well as the distance $E_g^{(k+1)}$ from the target function are calculated according to Eq. (10). The proposed configuration $f_g^{(k+1)}(\boldsymbol{r})$ is accepted with the probability p given by the Metropolis rule

$$p = \begin{cases} 1 & \text{if } E_g^{(k+1)} \leqslant E_g^{(k)} \\ \mathrm{e}^{(E_g^{(k)} - E_g^{(k+1)})/T} & \text{if } E_g^{(k+1)} > E_g^{(k)} \end{cases} \tag{11}$$

Otherwise, the old configuration is restored, i.e., $f_g^{(k+1)}(\boldsymbol{r}) = f_g^{(k)}(\boldsymbol{r})$. In Eq. (11), the symbol T represents the fictitious temperature of the system. As the temperature decreases, more changes that increase the distance $E_g^{(k)}$ from the target function are rejected. The reason for not rejecting all proposed changes when $E_g^{(k+1)} > E_g^{(k)}$ is to allow the system to evolve to the desired target configuration without being trapped in a local minimum of the distance from the target function give by Eq. (10); cf. Yeong and Torquato (1998a). Manwart *et al.* (2002) suggested implementing the exponentially decreasing fictitious temperature $T = T_0 \mathrm{e}^{-k/b}$, where T_0 and b are adjustable parameters. The reconstruction ends when the target characteristic is reached with a certain tolerance, or when a large number of successive proposed changes of $f_g^{(k)}(\boldsymbol{r})$ are rejected.

The selection of interfacial voxels (which have at least one neighbor that contains a different phase) as candidates $\boldsymbol{r}_1$ and $\boldsymbol{r}_2$ of an interchange significantly improves the rate of convergence of the simulated annealing algorithm (Rozman and Utz, 2001). The algorithm is versatile enough to allow the reconstruction of any multiphase media. Figure 4 illustrates the simulated annealing algorithm on the section of a reconstructed, spatially 3D cube.

2. *Poissonian Generation of Polydisperse Spheres*

Poissonian generation of polydisperse spheres is another technique for the reconstruction of porous media (Thovert *et al.*, 2001). This technique is useful for the reconstruction of media that result from the deposition of grains followed by their compaction, but it also allows the reconstruction of nongranular porous structures.

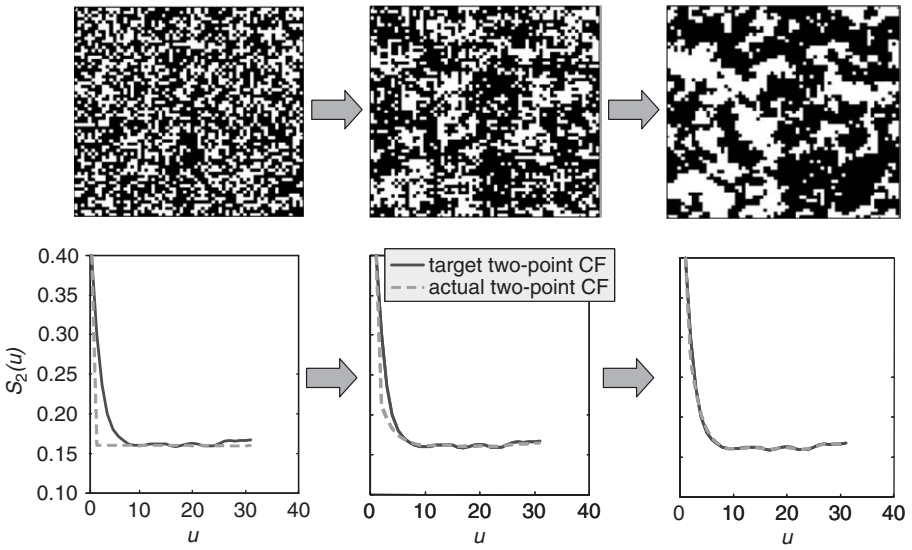

FIG. 4. Simulated annealing algorithm of the cube consisting of $65 \times 65 \times 65$ voxels starting from random initial condition (left), after 14×10^6 iterations (middle) and after 17×10^6 iterations (right). The two-point correlation function $S_2(u) = R(u)(\varepsilon - \varepsilon^2) + \varepsilon^2$ is compared with the target correlation function (CF) during the reconstruction.

For a porous medium represented by the phase function $f_g(\boldsymbol{r})$, we define the covering radius $r_c(\boldsymbol{r})$ of the solid phase as the radius of the largest sphere (or disk in 2D porous media) placed entirely into the solid phase and covering the point with coordinates $\boldsymbol{r}$. The value of r_c is zero inside the pores. The covering radius r_c can be found by the morphological operation called "opening," i.e., the erosion followed by the dilatation. The dilatation of the solid-phase domain $\boldsymbol{A}$ by the spherical element $\boldsymbol{B}_r$ with radius r is the set $\boldsymbol{A} \oplus \boldsymbol{B}_r$ covered by all translations of $\boldsymbol{B}_r$ centered in $\boldsymbol{A}$,

$$\boldsymbol{A} \oplus \boldsymbol{B}_r = \bigcup_{r \in \boldsymbol{A},\ s \in \boldsymbol{B}_r} (r + s) \tag{12}$$

The erosion is the dual operation, corresponding to all points in $\boldsymbol{A}$ not covered by a sphere $\boldsymbol{B}_r$ centered out of $\boldsymbol{A}$,

$$\boldsymbol{A} \ominus \boldsymbol{B}_r = (\boldsymbol{A}' \oplus \boldsymbol{B}_r)' \tag{13}$$

where the prime stands for the complement. The opening $\Phi(\boldsymbol{A}, r)$ is the result of an erosion followed by a dilatation

$$\Phi(\boldsymbol{A}, r) = (\boldsymbol{A} \ominus \boldsymbol{B}_r) \oplus \boldsymbol{B}_r \tag{14}$$

The important property of the opening $\Phi(\boldsymbol{A}, r)$ of the solid-phase domain $\boldsymbol{A}$ by the sphere/disk $\boldsymbol{B}_r$ of radius r is that it contains only points that can be covered by $\boldsymbol{B}_r$, because the components that were too small to contain $\boldsymbol{B}_r$ were removed by an erosion. The covering radius can thus be defined as

$$r_c(\boldsymbol{r}) = \sup\{r : \boldsymbol{r} \in \Phi(\boldsymbol{A}, r)\} \tag{15}$$

The integral distribution of the covering radius $G(r_c)$ is defined as

$$G(r_c) = (\text{Volume fraction of the set}) \{\boldsymbol{r} \in \boldsymbol{A}; r_c(\boldsymbol{r}) < r\} \tag{16}$$

and the limiting values of $G(r_c)$ are $G(0) = 0$ and $G(+\infty) = 1$, respectively. Graphically, the distribution $G(r_c)$ is the volume fraction of the solid phase, which cannot be covered by spheres (disks) of radius r_c.

The algorithm of the Poissonian generation of polydisperse spheres is simple (Thovert *et al.*, 2001). Spheres representing the solid phase are generated and randomly placed into the reconstruction domain until the desired porosity ε is reached. The distribution of the radii of generated spheres r corresponds to the spatially 3D distribution of the covering radius $G^{3D}(r_c)$ given by Eq. (16). In practice, the distribution of the covering radii can be evaluated either from the spatially 2D microscopy images (i.e., $G^{2D}(r_c)$) or from the spatially 3D solid-phase function obtained by computed micro-tomography or successive TEM imaging of sections of the porous medium (i.e., $G^{3D}(r_c)$). Clearly, the distributions $G^{2D}(r_c)$ and $G^{3D}(r_c)$ are generally different even for the same porous medium, and there is no unique mapping from $G^{2D}(r_c)$ into $G^{3D}(r_c)$ for general porous media.

If the spatially 3D distribution of the covering radii $G^{3D}(r_c)$ is not available, one has to reconstruct the porous medium from 2D distribution of covering radii $G^{2D}(r_c)$ evaluated from statistical analysis of microscopy images. The reconstruction algorithm then has to search for such a 3D distribution $G^{3D}(r_c)$ so that 2D distributions $G^{2D}(r_c)$ calculated from 2D sections of the reconstructed porous media match the $G^{2D}(r_c)$ obtained from microscopy images. As an example, the 2D phase function (white and black color states for solid phase and pores, respectively) and the corresponding calculated distribution of covering radii are shown in Figure 5.

3. *Thresholding of Correlated Random Fields*

Let us generate a spatially 3D isotropic porous medium $f_g(\boldsymbol{r})$ with a given porosity $\varepsilon = \overline{f_g(\boldsymbol{r})}$ and a given correlation function $R_g(u)$. The porous medium $f_g(\boldsymbol{r})$ is considered to be discretized into the grid of $N_c \times N_c \times N_c$ voxels, each voxel of the same size h. The reconstructed cube of the porous medium is usually considered to have periodic boundary conditions.

The random and discretized field $f_g(\boldsymbol{r})$ can be devised from a Gaussian field $X(\boldsymbol{r})$ discretized on the same $N_c \times N_c \times N_c$ grid, which is the starting point of

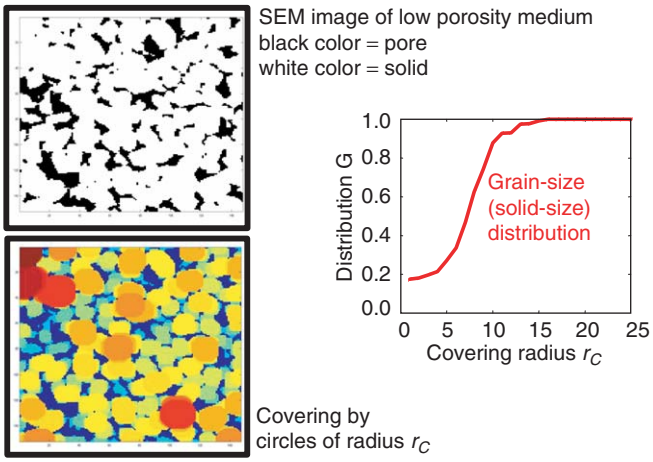

FIG. 5. Distribution of covering radius r_c. The solid phase of the porous medium is covered by circles of radius r_c and the color of circles depends on circle radius. The integral distribution of covering radius $G(r_c)$ is then displayed.

the algorithm and which is successively passed through the linear and nonlinear filters. The random variables in $X(\boldsymbol{r})$ are assumed to be normally distributed and are independent (i.e., not correlated). A linear operator can be defined by an array of coefficients $a(\boldsymbol{u}')$, where $\boldsymbol{u}'$ belongs to a finite cube, $\boldsymbol{u}' \in [0, L_c]^3$, and $L_c < (N_c h)$. A new random field $Y(\boldsymbol{r})$ can be expressed as a linear combination of the random variables $X(\boldsymbol{r})$,

$$Y(\boldsymbol{r}) = \sum_{\boldsymbol{u}' \in [0, L_c]^3} a(\boldsymbol{u}') X((\boldsymbol{r} + \boldsymbol{u}') \mathrm{mod}(N_c h)) \tag{17}$$

where the correlated random field $Y(\boldsymbol{r})$ is also discretized on the N_c^3 grid. Its correlation function $R_y(u)$ is calculated from the given correlation function $R_g(u)$ and from the porosity ε. The coefficients $a(\boldsymbol{u}')$ are obtained from the correlation function $R_y(u)$; cf. the details of the algorithm described by Adler and Thovert (1998). The particular choice of $a(\boldsymbol{u}')$ resulting in the Gaussian correlated random field is

$$a(u') = \exp\left(-\frac{\pi u'}{L_y^2}\right) \tag{18}$$

where L_y is the correlation distance (Mourzenko *et al.*, 2001).

Although the random field $Y(\boldsymbol{r})$ is correlated, it takes its values in the space of real numbers $\mathbb{R}$, while the porous medium has to be represented by a discrete-valued field $f_g(\boldsymbol{r})$. In order to create such a field from $Y(\boldsymbol{r})$, one applies a non-linear filter $f_g(r) = G(Y(\boldsymbol{r}))$, i.e., the random variable $f_g(\boldsymbol{r})$ is the deterministic

function of $Y(\boldsymbol{r})$. The nonlinear filter is realized by the introduction of the threshold t_ε,

$$f_g(\boldsymbol{r}) = \begin{cases} 1, & Y(\boldsymbol{r}) \leqslant t_\varepsilon \\ 0, & Y(\boldsymbol{r}) > t_\varepsilon \end{cases} \tag{19}$$

where the value of t_ε is adjusted so that the given porosity is satisfied, i.e., $\overline{f_g(\boldsymbol{r})} = \varepsilon$.

The thresholding of correlated random fields was generalized for the case of multiphase media by Losic *et al.* (1997). However, this reconstruction technique is limited only to cases where the third phase is located at the interface between two phases or within a single phase.

4. Reconstruction Based on Mechanical Diagenesis

An alternative to stochastic reconstruction of multiphase media is the reconstruction based on the direct simulation of processes by which the medium is physically formed, e.g., phase separation or agglomeration and sintering of particles to form a porous matrix. An advantage of this approach is that apart from generating a medium for the purpose of further computational experiments, the reconstruction procedure also yields information about the sequence of transformation steps and the processing conditions required in order to form the medium physically. It is thereby ensured that only physically realizable structures are generated, which is not necessarily the case when a stochastic reconstruction method such as simulated annealing is employed.

The mechanical routes of diagenesis usually represent particle packing in the force field, e.g., gravitational or electrostatic; cf. Fig. 6. Diagenesis-based reconstruction techniques have been used, e.g., by Kim *et al.* (2000) for the creation of model ceramic agglomerates by particle packing. Similarly, Kainourgiakis *et al.* (2002) have generated model porous media by ballistic deposition of spheres. Thomson and Gubbins (2000) generated model porous carbon structure by a reverse MC method. Formation of wet particle assemblies has also been represented by mechanical diagenesis (Kohout *et al.*, 2004).

There is of course a trade-off between the level of rigorosity of the diagenesis model and the computational cost (as well as the number of required input parameters). A qualitatively correct model is often sufficient for the purpose of porous/multiphase media reconstruction; a rigorous diagenesis model is required if the results are to be used, e.g., for process optimization.

E. Calculation of Effective Properties

1. Calculation of Effective Transport Properties on Reconstructed Porous Media

Calculation of the effective transport properties—thermal or electrical conductivity, effective diffusivity, and permeability—as a function of the

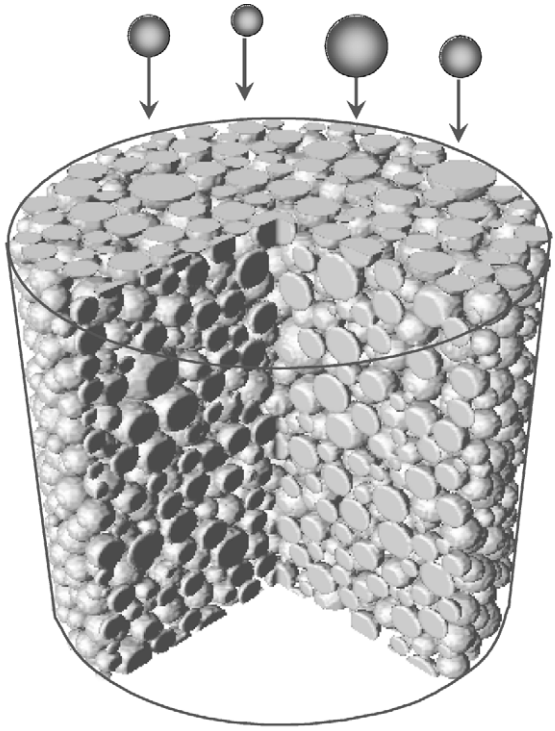

FIG. 6. Formation of the granular structure of the cylindrical pellet by the mechanism of sequential deposition of individual grains, the so-called ballistic packing.

microstructure of porous and multiphase media is of key interest for many chemical engineering applications as well as for other areas, such as geology (e.g., Dodds and Rothman, 2000; Sahimi, 1993). The general methodology for the calculation of effective transport properties from digitally reconstructed media is based on the local solution of transport equations followed by volume averaging (Quintard *et al.*, 1997; Whitaker, 1999), and can be summarized in the following steps:

(i) Microstructure characterization, as described in Section II.C.
(ii) Microstructure realization, as described in Section II.D.
(iii) Local solution of transport equations on the reconstructed medium with an imposed macroscopic gradient of temperature (for conductivity), concentration (for diffusivity), or pressure (for permeability).

(iv) Evaluation of the macroscopic transport parameter of interest (thermal conductivity, effective diffusivity, permeability) from converged temperature, concentration, or velocity fields according to the macroscopic transport laws.

These steps can then be iterated while a given morphological property of the medium (e.g., porosity or mean pore diameter) is systematically varied in order to generate structure–property correlations which can then be used in higher-level simulations either in the form of a look-up table, or fitted by an empirical correlation or theoretically founded function. The background to steps (i) and (ii) has already been discussed, so let us now consider steps (iii) and (iv) in detail. For an alternative analysis of the effective transport properties of disordered media based on the exit-time analysis, see Giona *et al.* (1995). It has to be noted that the four-step procedure outlined above is the direct computational analogy of experimental determination of transport properties. Step (ii) corresponds to the physical preparation of a sample, step (i) corresponds to its physicochemical characterization such as measurement of porosity, step (iii) corresponds to the physical measurement of transport rate (e.g., diffusion in a Wicke–Kahlenbach cell or heat flux in a guarded plate thermal conductivity meter), and step (iv) corresponds to the evaluation of the transport property of interest from "raw" mass- or heat-flux data.

The underlying problem of the calculation of transport properties is the numerical solution of the Poisson equation on a complex 3D domain defined by the phase functions. Several methods can be used, e.g., finite-difference discretization and the solution of the resulting linear system by the successive over-relaxation method (Kohout *et al.*, in press), the conjugate gradient method, or methods specifically suitable for solving large, sparse systems of linear algebraic equations. Heat conduction at steady state is governed by Fourier's law

$$\nabla \cdot (\lambda_i \nabla T) = 0 \tag{20}$$

where local values of thermal conductivity λ_i of each phase are used. At phase boundaries, the continuity of heat flux is required. A macroscopic temperature gradient $(T_2 - T_1)/L_z$ is imposed on the unit cell in a chosen direction (for isotropic media the choice of direction is not important), and the effective conductivity λ_e is obtained from the converged temperature field using macroscopic Fourier's law,

$$\lambda_e = -\frac{Q}{A}\frac{L_z}{T_2 - T_1} \tag{21}$$

where Q is the net steady-state heat flow rate obtained as a solution of Eq. (20), $A = L_x L_y$ the cross-sectional area of the unit cell perpendicular to the direction of the temperature gradient, and L_z the dimension of the unit cell in the direction of the temperature gradient (here z). The simulation setup is illustrated in Fig. 7.

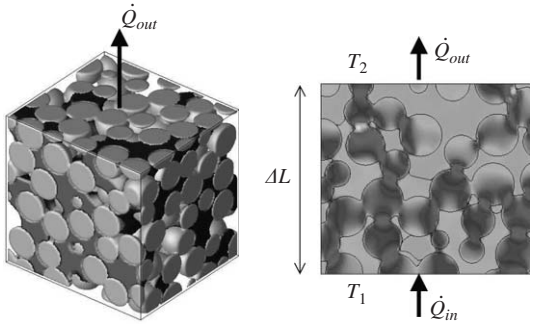

FIG. 7. Unit cell containing a wet particle packing for calculating the effective thermal conductivity. A cross-section showing the local heat fluxes at steady state (from Kohout *et al.*, 2004).

The dependence of conductivity on the composition and microstructure of porous media has been investigated, e.g., by Argento and Bouvard (1996) for sphere packing, or Roberts and Knackstedt (1996) for a range of model microstructures, including model solid foams. Effective thermal conductivity of two- and three-phase systems (solid-particle packing partially or fully saturated by a liquid phase) has recently been determined by Kohout *et al.* (2004) both computationally and experimentally. For a two-component system, consisting of particles of phase B dispersed in a continuous phase A, λ_e as function of the phase volume fraction ϕ_B was confirmed to observe Archie's-like power law

$$\lambda_e = (\lambda_B - \lambda_A)\phi_B^c + \lambda_A \tag{22}$$

where λ_A and λ_B are component conductivities, and the exponent c is a function of the ratio λ_B/λ_A and of the microstructure. Simulation results for the case of spherical particles are plotted in Fig. 8. For spherical particles, it was found that $c = 0.136\log(\lambda_B/\lambda_A) + 1.27$ and for cubic particles $c = 0.239\log(\lambda_B/\lambda_A) + 1.10$ (Kohout *et al.*, 2004). These correlations are valid in the range $2 < \lambda_B/\lambda_A < 100$ and $0.5 < \phi_B < 0.7$ for spheres, and $0.0 < \phi_B < 1.0$ for cubes.

Calculation of the effective diffusivity is analogous to that of conductivity. The steady-state Fick's law

$$\nabla \cdot (D_i \nabla c) = 0 \tag{23}$$

is solved in the unit cell, where D_i is the diffusion coefficient in phase i and c is the concentration. In a multiphase medium, the diffusivities in some of the phases may be zero. A macroscopic concentration gradient $(c_2 - c_1)/L_z$ is imposed on the unit cell in a chosen direction and Eq. (23) is solved. The effective diffusivity is then evaluated from the macroscopic Fick's law

$$D_e = -\frac{J}{A}\frac{L_z}{c_2 - c_1} \tag{24}$$

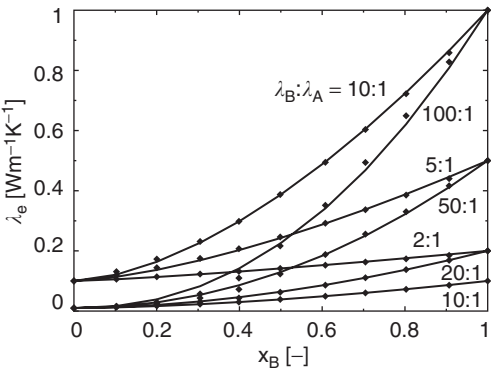

FIG. 8. Dependence of effective thermal conductivity of a two-phase medium A–B (randomly positioned overlapping spheres of phase B in continuous phase A) on the ratio of component conductivities (from Kohout *et al.*, 2004).

where J/A is the steady-state diffusive flux obtained as a solution of Eq. (23). If diffusion occurs through only one phase with diffusion coefficient D_i, the dimensionless ratio D_e/D_i, sometimes also called the formation factor, can be correlated with the phase volume fraction of the phase, ϕ_i, and the tortuosity factor τ of the porous medium can also be evaluated from $D_e = D_i\phi_i/\tau$. Recent examples of effective diffusivity studies in porous media or porous media filled with two fluid phases are provided, e.g., by Kainourgiakis *et al.* (2002), Nam and Kaviany (2003), and Galani *et al.* (2004).

In microporous materials where Knudsen diffusion prevails, D_e cannot be calculated by solving Fick's law. The use of a discrete particle simulation method such as dynamic MC is appropriate in such cases (Coppens and Malek, 2003; Zalc *et al.*, 2003, 2004). In the Knudsen regime, relatively few gas molecules collide with each other compared with the number of collisions between molecules and pore walls. One of the fundamental assumptions of the Knudsen diffusion is that the direction in which a molecule rebounds from a pore wall is independent of the direction in which it approaches the wall, and is governed by the cosine law: the probability ds that a molecule leaves the surface in the solid angle dω forming an angle θ with the normal to the surface is

$$\mathrm{d}s = (\mathrm{d}\omega/\pi)\cos\theta \tag{25}$$

The theoretical basis for the cosine distribution of velocities remained unclear for a long time. Feres and Yablonsky (2004) introduced a simple model that considers the surface of the pores to have some micro-roughness, and employ the random billiard model for individual molecules. In this model, gas molecules move freely inside a region of space until they collide elastically with a rough surface and instantaneously rebound according to the usual law of equal angles of incidence and reflection. Geometrical irregularities of the surface naturally

make the angle of reflection sensitive to the precise point at which a collision takes place. As the scale of surface irregularities is reduced, the deterministic but highly unstable angle of reflection becomes effectively random. Its probability law, however, is still a function of the (scale-independent characteristics of the) surface geometry. Feres and Yablonsky (2004) show that the Knudsen cosine law (25) is a stationary probability distribution of post-collision scattered directions (velocities) of gas molecules.

Permeability is calculated by imposing a macroscopic pressure gradient across the unit cell and solving the Stokes and continuity equations in the pore space

$$\nabla p = \eta \nabla^2 \boldsymbol{u}, \qquad \nabla \cdot \boldsymbol{u} = 0 \tag{26}$$

where p is the pressure, η the viscosity, and $\boldsymbol{u}$ the velocity vector, with no-slip boundary conditions on the solid walls. This procedure can be regarded as the computational equivalent of gas permeation experiments (Capek *et al.*, 2001). In partially saturated porous media (e.g., water–air and water–oil), each liquid phase can be considered stationary and the relative permeability of the other phase calculated as a function of its relative pore-space saturation, or a two-phase flow problem can be solved and the relative permeabilities of the two phases determined simultaneously. The permeability κ_0 is obtained from converged velocity profile (Fig. 9) using the macroscopic Darcy's law

$$\kappa_0 = -\eta \frac{U}{A} \frac{L_z}{p_2 - p_1} \tag{27}$$

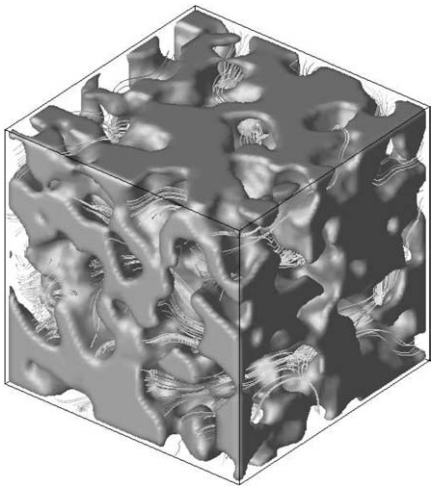

FIG. 9. Streamlines showing steady-state velocity profile during single-phase flow in a reconstructed porous medium.

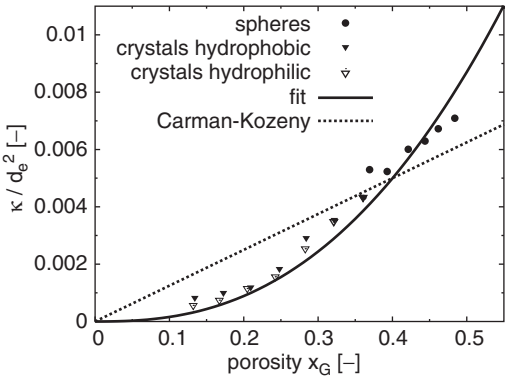

FIG. 10. Dependence of relative permeability of gas phase on the volume fraction of gas phase for dry and partially water-saturated porous media of various morphology, fitted by a power-law function and compared with the Carman–Kozeny equation (from Kohout *et al.*, in press).

where U is the imposed macroscopic volume flowrate (U/A is superficial velocity), and $(p_2 - p_1)$ the pressure drop across the unit cell. For the purpose of structure–property correlations, permeability is typically scaled by the square of the equivalent hydraulic diameter d_e^2 defined following Eq. (4). An example of calculated dependence of the relative permeability of the gas phase on porosity of random packings of spherical and rectangular particles partially saturated by wetting and non-wetting liquid is shown in Fig. 10 (Kohout *et al.*, in press).

2. *Calculation of Tensile Properties*

The relationship between the structure of the disordered heterogeneous material (e.g., composite and porous media) and the effective physical properties (e.g., elastic moduli, thermal expansion coefficient, and failure characteristics) can also be addressed by the concept of the reconstructed porous/multiphase media (Torquato, 2000). For example, it is of great practical interest to understand how spatial variability in the microstructure of composites affects the failure characteristics of heterogeneous materials. The determination of the deformation under the stress of the porous material is important in porous packing of beds, mechanical properties of membranes (where the pressure applied in membrane separations is often large), mechanical properties of foams and gels, etc. Let us restrict our discussion to equilibrium mechanical properties in static deformations, e.g., effective Young's modulus and Poisson's ratio. The calculation of the impact resistance and other dynamic mechanical properties can be addressed by discrete element models (Thornton *et al.*, 1999, 2004).

The stress tensor $\boldsymbol{\sigma}$ in the perfectly elastic and isotropic solid phase of the porous medium is described by the constitutive equation

$$\boldsymbol{\sigma} = \lambda(\nabla \cdot \boldsymbol{d})\boldsymbol{I} + \mu(\nabla \boldsymbol{d} + (\nabla \boldsymbol{d})^{\mathrm{T}}) \tag{28}$$

where λ and μ are the Lamé coefficients, and $\boldsymbol{d}$ the displacement that characterizes the deformation of the solid phase. The condition of elastostatic equilibrium in the absence of external body forces $\nabla \cdot \boldsymbol{\sigma} = \mathbf{0}$ can be formulated with the above definition of the stress tensor as

$$(\lambda + \mu)\nabla(\nabla \cdot \boldsymbol{d}) + \mu\nabla^2 \boldsymbol{d} = \mathbf{0} \tag{29}$$

The boundary condition at the solid–pore interphase S_p has to be supplemented as $\boldsymbol{\sigma} \cdot \boldsymbol{n} = \boldsymbol{T}$, that is

$$[\mu(\nabla \boldsymbol{d} + (\nabla \boldsymbol{d})^{\mathrm{T}}) + \lambda(\nabla \cdot \boldsymbol{d})\boldsymbol{I}] \cdot \boldsymbol{n} = \boldsymbol{T} \quad \text{on } S_p \tag{30}$$

where $\boldsymbol{n}$ is the unit normal of the solid phase and $\boldsymbol{T}$ the surface traction.

Let us consider the spatially periodic porous medium consisting of an infinite number of identical unit cells. The spatially periodic medium is subjected to a macroscopic deformation described by the tensor of deformation $\boldsymbol{A}$, and the local displacement $\boldsymbol{d} = \boldsymbol{A} \cdot \boldsymbol{x} + \tilde{\boldsymbol{d}}$ can be decomposed into a macroscopic deformation $\boldsymbol{A} \cdot \boldsymbol{x}$ and a microscopic spatially periodic displacement $\tilde{\boldsymbol{d}}$; cf. Poulet *et al.* (1996). This decomposition introduced into elastostatic Equations (29) and (30) yields

$$(\lambda + \mu)\nabla(\nabla \cdot \tilde{\boldsymbol{d}}) + \mu\nabla^2 \tilde{\boldsymbol{d}} = \mathbf{0} \tag{31}$$

$$\begin{aligned} &[\mu(\nabla \tilde{\boldsymbol{d}} + (\nabla \tilde{\boldsymbol{d}})^{\mathrm{T}}) + \lambda(\nabla \cdot \tilde{\boldsymbol{d}})\boldsymbol{I}] \cdot \boldsymbol{n} \\ &\quad = -\mu(\boldsymbol{A} + \boldsymbol{A}^{\mathrm{T}}) \cdot \boldsymbol{n} - \lambda(\mathrm{tr}\, \boldsymbol{A})\boldsymbol{n} + \boldsymbol{T} \quad \text{on } S_p \end{aligned} \tag{32}$$

Hence, the macroscopic deformation $\boldsymbol{A}$ plays the role of an external "driving force." The macroscopic stress $\langle \boldsymbol{\sigma} \rangle$ can be defined as the average local stress over the solid portion V_s of the unit cell

$$\langle \boldsymbol{\sigma} \rangle = \frac{1}{V} \int_{V_s} \sigma \, \mathrm{d}V \tag{33}$$

where V is the total volume of the unit cell. When the porous medium is isotropic, the macroscopic stress is given by

$$\langle \boldsymbol{\sigma} \rangle = \lambda_e \, \mathrm{tr}\, \boldsymbol{E} \cdot \boldsymbol{I} + 2\mu_e \boldsymbol{E} \tag{34}$$

where λ_e and μ_e are effective Lamé coefficients of the medium and $\boldsymbol{E} = \frac{1}{2}(\boldsymbol{A} + \boldsymbol{A}^{\mathrm{T}})$ the macroscopic strain. The effective Young's modulus E_e and the effective Poisson's ratio ν_e are related to effective Lamé coefficients as $E_e = \mu_e(3\lambda_e + 2\mu_e)/(\lambda_e + \mu_e)$ and $\nu_e = \lambda_e/(2(\lambda_e + \mu_e))$, respectively.

F. Effective-scale Transport Models

Effective-scale models make no specific assumption about the geometry of the pore space, and the reaction-transport equations are formulated with the concentration field averaged over a certain effective spatial scale. All the effective-scale models use in general the so-called tortuosity τ as a fitting parameter. The tortuosity can be related to the geometry of the pore space, cf. Section II.C, but it lumps too much information to be used as a single characteristic of the porous medium, because it depends also on pressure and on the actual set of diffusing gases (Aris, 1975; Bhatia, 1986; Jackson, 1977).

The constitutive equations of transport in porous media comprise both physical properties of components and pairs of components and simplifying assumptions about the geometrical characteristics of the porous medium. Two advanced effective-scale (i.e., space-averaged) models are commonly applied for description of combined bulk diffusion, Knudsen diffusion and permeation transport of multicomponent gas mixtures—Mean Transport-Pore Model (MTPM)—and Dusty Gas Model (DGM); cf. Mason and Malinauskas (1983), Schneider and Gelbin (1984), and Krishna and Wesseling (1997). The molar flux intensity of the ith component $\boldsymbol{N}_i$ is the sum of the diffusion $\boldsymbol{N}_i^{\mathrm{d}}$ and permeation $\boldsymbol{N}_i^{\mathrm{p}}$ contributions,

$$\boldsymbol{N}_i = \boldsymbol{N}_i^{\mathrm{d}} + \boldsymbol{N}_i^{\mathrm{p}}, \quad i = 1, \ldots, n \tag{35}$$

In the DGM, the solid phase is modeled as giant dust molecules held motionless in space with which the diffusing gas molecules collide. The constitutive equations governing the diffusion molar flux intensities $\boldsymbol{N}_i^{\mathrm{d}}$ for both MTPM and DGM are the generalized Maxwell–Stefan equations

$$\frac{\boldsymbol{N}_i^{\mathrm{d}}}{D_i^{\mathrm{K}}} + \sum_{i=1, j\neq i}^{\mathrm{n}} \frac{y_j \boldsymbol{N}_i^{\mathrm{d}} - y_i \boldsymbol{N}_j^{\mathrm{d}}}{D_{ij}^{\mathrm{eff}}} = \begin{cases} -c_{\mathrm{T}} \nabla y_i & \text{MTPM} \\ -\nabla (c_{\mathrm{T}} y_i) & \text{DGM} \end{cases} \tag{36}$$

for $i = 1, \ldots, n$, where y_i is the mole fraction of the ith component, c_{T} the total concentration, $D_{\mathrm{ij}}^{\mathrm{eff}} = \psi D_{ij}$ the effective binary diffusion coefficient, D_{ij} the binary bulk diffusion coefficient, and ψ the geometrical factor formally defined as the ratio of porosity ε and tortuosity τ, $\psi = \varepsilon/\tau$. Parameter $D_i^{\mathrm{K}} = \psi \langle r \rangle \mathrm{K}_i$ is the effective Knudsen diffusivity of the ith component, where the Knudsen coefficient is $\mathrm{K}_i = \frac{2}{3}\sqrt{8RT/(\pi M_i)}$, $\langle r \rangle$ the mean pore radius, R the gas constant, T the temperature, and M_i the molecular weight of the ith component.

Both MTPM and DGM share the Darcy's constitutive equation governing the permeation molar flux intensity of the ith component $\boldsymbol{N}_i^{\mathrm{p}}$,

$$\boldsymbol{N}_i^{\mathrm{p}} = -y_i \kappa_i \nabla c_{\mathrm{T}} = -\frac{y_i \kappa_i}{RT} \nabla p, \quad i = 1, \ldots, n \tag{37}$$

where κ_i is the effective permeability coefficient of the ith component. In the case of DGM, all effective permeability coefficients are identical, i.e., $\kappa = \kappa_1 = \ldots = \kappa_n$:

$$\kappa = \kappa_0 p/\eta \tag{38}$$

where η is the dynamic viscosity and κ_0 the Darcy's permeability. For cylindrical pores with mean square pore radius $\langle r^2 \rangle$, the parameter κ_0 can be formally replaced by $\kappa_0 = \psi \langle r^2 \rangle / 8$. A number of correlations are available to estimate κ_0, e.g., the popular Carman–Kozeny equation applicable for the aggregated bed of spheres. MTPM assumes that the decisive part of the gas transport takes place in transport pores that are considered to be cylindrical capillaries distributed around the mean value $\langle r \rangle$. The width of this distribution is characterized by the mean value of the squared transport-pore radii $\langle r^2 \rangle$. Effective permeability κ can be in the case of the single component permeation described by MTPM approximated by the Weber equation

$$\kappa = \langle r \rangle \psi \mathrm{K} + \langle r^2 \rangle \psi p/(8\eta) \tag{39}$$

where K is the Knudsen number.

The DGM by Mason and Malinauskas (1983) is the frequently used alternative to effective Fick's diffusion for the calculation of the multicomponent diffusion and convection in the porous media. A number of special features of multicomponent diffusion and convection in the pore space have been outlined by Krishna (1993).

III. Transformations

The microstructure of the multiphase media is often the product of phase transitions, e.g. (i) capillary condensation in the porous media, (ii) phase separation in polymer/polymer and polymer/solvent systems, (iii) nucleation and growth of bubbles in the porous media, (iv) solidification of the melt with a temporal three-phase microstructure (solid, melt, gas), and (v) dissolution, crystallization or precipitation. The subject of our interest is not only the topology of the resulting microstructured media, but also the dynamics of its evolution involving the formation and/or growth of new phases.

The structure of the porous media can also be shaped by mechanical and electrostatic forces, e.g., sheeting of granules at conveyor walls (Yao *et al.*, 2004), deposition of solid grains in the porous media, and fragmentation of catalyst carriers. Simple examples of mechanical diagenesis of porous media were already illustrated in Section II.D.4. In this section, we first describe the morphological operation of skeletonization and the methods used for the

simulation of various phase transitions, and then discuss the modeling of chemically reactive systems.

A. Skeletonization

Let us first discuss the mapping from the phase function defined in Section II.A into the pore-network diagram. The analysis of the network connectivity of the pore (or solid) phase can be based on the construction of skeleton its (Thovert *et al.*, 1993). In the skeletonization of the porous phase, the elements of the object are removed until only the skeleton remains. This process is called "thinning" in the terminology of mathematical morphology. The constructed skeleton of the pore phase allows the analysis of its topological characteristics, and the determination of the connected and percolating components of the porous phase, e.g., transport or dead-end pores. Liang *et al.* (2000b) extracted the skeleton of pore space using an improved parallel thinning algorithm introduced by Ma and Sonka (1996). Once the skeleton is obtained, its vertices and edges can be identified as well as the minima in the cross-sectional area of pores along the skeleton branches, which correspond to bottlenecks of the pore space.

We applied a skeletonization method not to the pore space, but to the solid phase in order to find the bottlenecks of the skeleton of the solid phase (Grof *et al.*, 2003). An illustrative example of the object and its skeleton is shown in Fig. 11. We employed the fully parallel 3D thinning algorithm described by Ma and Sonka (1996) that preserves the original connectivity of the processed phase. During the thinning, an object element is removed if its neighborhood satisfies any of the deleting templates, and the thinning ends when no additional object element can be removed. The elements of a resulting skeleton can then be classified as

(1) *Line-end elements* if they have only one neighboring element.
(2) *Edge elements* if they have two neighboring elements.
(3) *Vertices elements* if they have three or more neighboring elements.

The cross-sectional area of the solid phase perpendicular to the skeleton edge is calculated along all skeleton branches of the solid phase. The solid phase is then disconnected at the points corresponding to the absolute minima of that cross-sectional area for every skeleton edge (branch); cf. Grof *et al.* (2003). Examples of solid-phase fragments of the porous media formed by the disconnection of the solid-phase skeleton at weak points are shown in Figures 11 and 12.

B. Phase Transitions

1. Free Surface and Interfacial Flows

Simulation of free-surface and interfacial flows is a topic with many practical applications, e.g., the formation of droplet clouds or sprays from liquid jets,

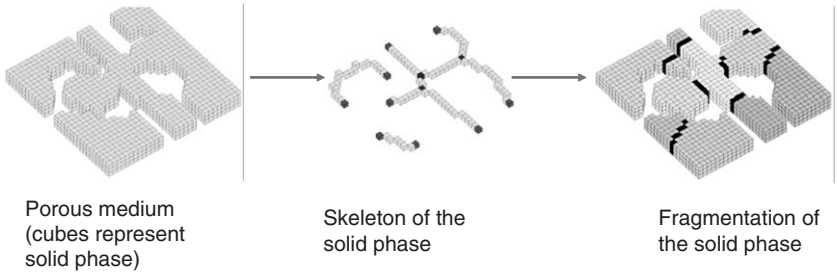

FIG. 11. Schema of skeletonization of porous media by the algorithm of conditional thinning and disconnection of the skeleton at the weak points to predict the location of fractures. Classification of skeleton elements according to number of neighboring elements: line-ends (1 neighboring element), edges (2), vertices (3 and more) (from Grof *et al.*, 2003).

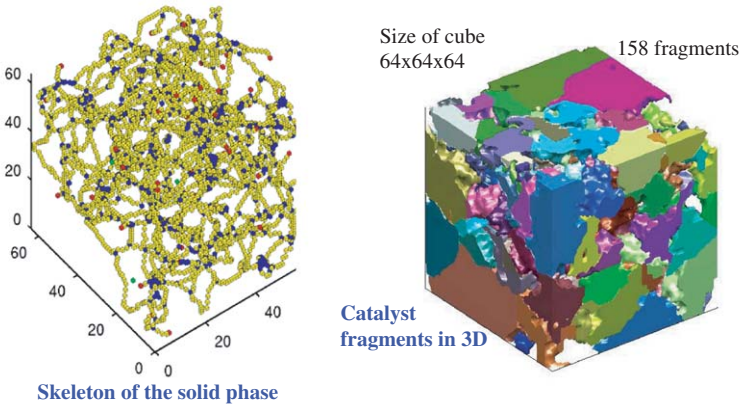

FIG. 12. Skeleton of the the solid phase of spatially 3D reconstructed porous medium obtained by conditional thinning and disconnection of the skeleton at the weak point (from Grof *et al.*, 2003).

collision of liquid droplets, capillary condensation in pores, dissolution of porous granules, and drying (Kohout *et al.*, in press). Major difficulties in simulations are associated with the change of the interface topology that occurs during the coalescence or breakup of droplets.

Simulation methods for problems with free surfaces governed by Navier–Stokes equations were reviewed by Scardovelli and Zaleski (1999). The specific problems of these simulations are the location of the interface and the choice of the spatial discretization:

- In *fixed-grid methods*, there is a predefined grid that does not move with the interface. The interface has to somehow cut across this structured or unstructured fixed grid. The popular Volume of Fluid (VOF), Level Set (Sethian, 1996) or cellular automata methods are examples of a fixed-grid approach.

- In *moving-grid methods*, the interface is a boundary between two subdomains of the grid. The interface then identifies, at some order of approximation, with boundaries of elements into which the phases are discretized. When the interface undergoes large deformations, the grid has to be remeshed.
- In *particle-technique methods*, no grids are needed. The liquid is considered to be discretized into number of particles with force interacting among individual particles (Heyes *et al.*, 2004).

Let us introduce the VOF method in more detail. The phase volume function $\hat{f}_1(\boldsymbol{r})$ is defined by $\hat{f}_1 = 1$ in phase 1 and $\hat{f}_1 = 0$ in phase 2; cf. Eq. (1). A discrete analog of the phase volume function $\hat{f}_1$ is the scalar field ϕ_1 known as the volume fraction (or area fraction in spatially 2D cases). It represents the fraction of the volume of the voxel with size h and the coordinate of its center $\boldsymbol{r}$ filled with the phase 1,

$$\widehat{\phi}_1 = \frac{1}{h^3} \int_{\boldsymbol{u} \in [-h/2, h/2]^3} \widehat{f}_1(\boldsymbol{r} + \boldsymbol{u}) \, \mathrm{d}\boldsymbol{u} \tag{40}$$

where a cubic mesh with a constant grid spacing h is considered. We have $0 < \widehat{\phi}_1 < 1$ in cells cut by the interface S and $\widehat{\phi}_1 = 0$ or 1 away from it. In the incompressible flow, mass conservation is equivalent to conservation of the volume and hence of the characteristic function $\widehat{\phi}_1$. In the VOF method, the algorithmic scheme is local in the sense that only the $\widehat{\phi}_1$ values, pressure, and velocity field of the neighboring cells are needed to update the $\widehat{\phi}_1(\boldsymbol{r})$ value in the voxel with coordinates $\boldsymbol{r}$. For this reason, it is relatively simple to implement these algorithms in parallel and, in particular, within the framework of domain decomposition techniques.

The central problem of the VOF method is the reconstruction and representation of the interface. For example, in two spatial dimensions, the interface is considered to be a continuous, piecewise smooth line; the problem of its reconstruction is that of finding an approximation to the section of the interface in each cut cell by knowing only the volume fraction $\widehat{\phi}_1$ in that cell and in the neighboring ones.

2. *Capillary Condensation in Porous Media*

Operations like pressure swing adsorption involve the condensation of the liquid in the porous medium. Several researchers developed predictive models of the configuration of liquid phase in the wet, unsaturated, porous media. The method developed by Silverstein and Fort (2000) is based on simulated annealing with random swapping of gas and liquid elements in the system to achieve a global energy minimum defined by

$$G_{\mathrm{t}}^{\mathrm{s}} = \sum_i A_i \gamma_i \tag{41}$$

where i represents the interface, G_t^s the total interfacial free energy of the system, A_i the area of the interface, and γ_i the interfacial free energy of the interface. As a result of interfacial tension, the system tends to minimize surface area A for a given volume of condensate V, and this minimization is subjected to the Kelvin equilibrium and wetting angle constraints. The Kelvin equation relates the interface curvature radius r and the equilibrium vapor pressure above it p^*,

$$p^* = p_s \exp\left[-\frac{2\gamma}{r}\frac{V_m}{RT}\right] \tag{42}$$

Here p_s is the saturated vapor pressure at temperature T, γ the surface tension, V_m the molar volume of the liquid, and the curvature radius r is conventionally taken as negative for concave interfaces. Kelvin equation for a non-ideal multicomponent mixture was derived by Shapiro and Stenby (1997).

Stepanek *et al.* (1999) presented an algorithm for tracking the evolution of liquid–vapor interfaces moving with curvature-dependent velocity so as to reach an equilibrium shape, which represents the local minimum of a global Gibbs energy. Their algorithm is derived from the level-set approach (Sethian, 1996), and was applied to the modeling of capillary condensation hysteresis cycles in reconstructed porous media. Concave interfaces tend to evaporate spontaneously, while either condensation or evaporation can occur on a convex interface, depending on its curvature and the total pressure and composition of the vapor phase. Interface displacements are curvature-dependent; the curvature radius r is calculated by locally approximating the interface by an elliptic paraboloid oriented so that its axis is identified with the liquid–gas interface normal vector given by Eq. (6).

In the algorithm of Stepanek *et al.* (1999), the simulated domain is discretized into a set of cubic volume elements; the phase-encoding alphabet is $A = \{s, l, f, g\}$ (meaning solid, liquid, interface, and gas, respectively). In addition, a value $\widehat{\phi}_i \in (0, 1)$ expressing the volume fraction of condensate in the ith discretization element (i.e., its saturation) is assigned to every interface element. The driving force of the interface growth in terms of the partial pressure, $||p - p^*|| \leqslant p_\varepsilon$, was used as a convergence criterion of the algorithm. The parameter p_ε has a physical meaning of the potential barrier to phase transition, which reveals itself by the existence of oversaturated vapors and metastable liquids.

3. *Formation of Gas Cavities in Liquid-saturated Porous Medium*

The formation of gas bubbles in a porous medium affects, e.g., the performance of anaerobic granular sludge particles containing entrapped gas (wastewater treatment), or the performance of electrochemical reactors where a gas (hydrogen, oxygen, chlorine) evolves inside a porous electrode. A related problem is that of bubble nucleation on structure surfaces, which can be as varied as specially designed surfaces for enhanced nucleate boiling heat transfer, or the

wall of a champagne glass (Liger-Belair *et al.*, 2002). In porous media, patterns and rates of gas evolution are different than in the bulk phase because of the heterogeneous nucleation. Moreover, the solute transport, capillary and viscous forces affect the growth of gas bubbles in the porous media (Dominquez *et al.*, 2000). The first model of the bubble growth in the porous medium driven by a constant or a time-varying supersaturation in the far field was presented by Li and Yortsos (1995). The porous medium was represented in their study by an equivalent network of nodes (pore bodies) and bonds (pore throats) of distributed sizes.

According to the Young–Laplace equation, a pressure difference Δp is required to support a stable, curved interface with curvature radii r_1 and r_2 (by convention, positive for convex interfaces and negative for concave ones),

$$\Delta p = p_g - p_l = \sigma\left(\frac{1}{r_1} + \frac{1}{r_2}\right) \tag{43}$$

Another condition that has to be satisfied by a stable gas cavity existing in the pore space is that the solid wall and the gas–liquid phase boundary must join at a certain contact angle ϑ, which depends on the wettability of the solid phase.

Stepanek *et al.* (2001b) developed an algorithm for finding a configuration of gaseous and liquid phases in a porous medium, satisfying certain curvature at all gas–liquid interfaces and a predefined contact angle at all gas–liquid–solid contact lines; cf. Fig. 13. Their algorithm is based on a modified level-set

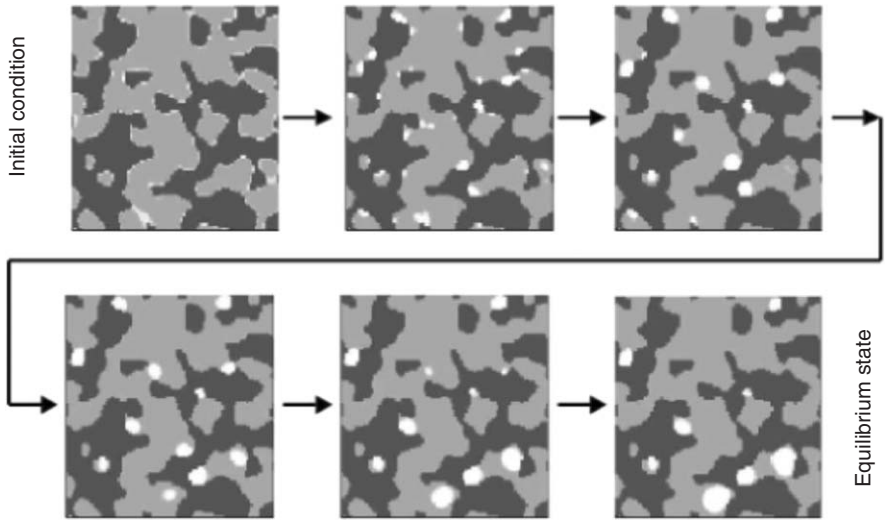

FIG. 13. Simulation of bubble growth and coarsening in a water-saturated porous medium (from Stepanek *et al.*, 2001b).

method for the tracking of moving interfaces propagating with curvature-dependent velocity (Stepanek *et al.*, 1999). The saturation of gas–liquid interface voxels described by the saturation function $g_i \in (0;1)$ is updated according to $\mathrm{d}g_i = \alpha(p_1/\eta)(1-p_1^*)\,\mathrm{d}t$, where α is a numerical parameter determining the rate of convergence and stability η the viscosity of the liquid, and $p_1^* = p_g' - \sigma'(1/r_1' + 1/r_2')$, with $p_g' = p_g/p_1$ using the gas over-pressure, $\sigma' = \sigma/(ap_1)$ a dimensionless capillary pressure, and r_1' and r_2' are the estimates of the interface curvature radii.

4. *Solidification of Melts*

Microstructure evolution in solids formed from a melt is important in processes such as prilling or casting. For example, in aluminum alloy shape casting the final microstructure depends directly on the as-cast microstructure since the only post-casting process is the heat treatment. The micro-porosity formed owing to the combined effects of the volumetric shrinkage upon the solidification of the melt and the precipitation of the dissolved hydrogen affects the final properties of the aluminum alloy.

A solidification model of the aluminum melt was proposed by Atwood and Lee (2003) and by Lee *et al.* (2004), and consists essentially of the grain growth and pore growth sub-models. The nucleation and growth of the solid phase and gas bubbles simulated by the cellular automata method, whereas the multi-component diffusion and partitioning in a three-phase system (liquid melt, solid grains, and gas) are simulated by a finite difference method. The driving force in the cellular automata algorithm for both the nucleation and growth of the solid phase is the local under-cooling. Hence, the heat balance equations at the macro-scale are required. When the amount of the solid in a voxel increases, the dissolved solutes are partitioned between the solid and liquid phases. The change in the solute concentration affects the degree of under-cooling and, hence, the nucleation and growth processes. Similarly, a pore may form in a voxel by a nucleation event, and a pore may expand into a neighboring cell if the concentration of hydrogen in the melt favors it.

5. *Spinodal Decomposition*

Nauman and He (2001) considered the modeling of the formation of two-phase morphologies by the spinodal decomposition of the initially homogeneous polymer/polymer or polymer/solvent mixture that was thermally quenched into a two-phase region. Let us outline their modeling approach.

Fick's diffusion cannot be applied to the description of the evolution of multiphase systems because it acts to smooth concentration differences and drives the system toward the uniform concentration profiles of species. Instead of Fick's diffusion, where the concentration gradient acts as a driving force, the intensity of the diffusion flux $\boldsymbol{N}_A$ of the species A can be considered to be

proportional to the gradient of the chemical potential

$$\boldsymbol{N}_{\mathrm{A}} = -D\,\frac{\phi_{\mathrm{A}}}{RT}\,\nabla\mu_{\mathrm{A}} \tag{44}$$

where D is the diffusion coefficient, ϕ_{A} the mole (or volume) fraction, and μ_{A} the chemical potential of component A. Let g_{mix} be the free energy of mixing of the binary mixture. Then the chemical potential of component A is $\mu_{\mathrm{A}} = g_{\mathrm{mix}} + (1-\phi_{\mathrm{A}})(\partial g_{\mathrm{mix}}/\partial\phi_{\mathrm{A}})$. The local balance of species A corresponding to Eq. (44) is

$$\frac{\partial\phi_{\mathrm{A}}}{\partial t} = \nabla\cdot\left[D\,\frac{\phi_{\mathrm{A}}(1-\phi_{\mathrm{A}})}{RT}\,\frac{\partial^2 g_{\mathrm{mix}}}{\partial\phi_{\mathrm{A}}^2}\,\nabla\phi_{\mathrm{A}}\right] = \nabla\cdot(D^{\mathrm{eff}}\nabla\phi_{\mathrm{A}}) \tag{45}$$

where D^{eff} is the effective diffusion coefficient. Let us assume that the Gibbs free energy g_{mix} of the polymer/polymer or polymer/solvent system is described by the Flory–Huggins equation

$$\frac{g_{\mathrm{mix}}}{RT} = \frac{\phi_{\mathrm{A}}\ln\phi_{\mathrm{A}}}{N_{\mathrm{A}}} + \frac{(1-\phi_{\mathrm{A}})\ln(1-\phi_{\mathrm{A}})}{N_{\mathrm{B}}} + \chi\phi_{\mathrm{A}}(1-\phi_{\mathrm{A}}) \tag{46}$$

where N_{A} and N_{B} are dimensionless numbers chosen to reflect relative molecular size and χ the interaction parameter. Substituting from Eq. (46) into Eq. (45) gives the effective diffusion coefficient

$$D^{\mathrm{eff}} = D\left[\frac{\phi_{\mathrm{A}}N_{\mathrm{A}} + (1-\phi_{\mathrm{A}})N_{\mathrm{B}}}{N_{\mathrm{A}}N_{\mathrm{B}}} - 2\phi_{\mathrm{A}}(1-\phi_{\mathrm{A}})\chi\right] \tag{47}$$

The effective diffusion coefficient becomes negative for some range of composition when χ is sufficiently large. The separation of phases requires an up-hill diffusion (characterized by negative D^{eff}) in which the material moves against concentration gradients. The kinetics of the separation and the morphology of separated phases depend on the details of such diffusion.

For a system to exhibit two-phase behavior, it is necessary that $g_{\mathrm{mix}}(\phi_{\mathrm{A}})$ has two minima within $0<\phi_{\mathrm{A}}<1$. The points near the minima of $g_{\mathrm{mix}}(\phi_{\mathrm{A}})$ are called the binodal points, $\phi_{\mathrm{A}}^{\mathrm{l}} < \phi_{\mathrm{A}}^{u}$, and are given by the condition $g'_{\mathrm{mix}}(\phi_{\mathrm{A}}^{\mathrm{l}}) = g'_{\mathrm{mix}}(\phi_{\mathrm{A}}^{u})$, where the derivative $g'_{\mathrm{mix}} = \partial g_{\mathrm{mix}}/\partial\phi_{\mathrm{A}}$. The condition of two minima of $g_{\mathrm{mix}}(\phi_{\mathrm{A}})$ implies $g''_{\mathrm{mix}}(\phi_{\mathrm{A}}) = \partial^2 g_{\mathrm{mix}}/\partial\phi_{\mathrm{A}}^2 < 0$ for some interval within $0<\phi_{\mathrm{A}}<1$. The points $\phi_{\mathrm{A}}^{\mathrm{sl}}$ and ϕ_{A}^{su}, where $g''_{\mathrm{mix}}(\phi_{\mathrm{A}}) = 0$, are the spinodal points, and the region between these points is thermodynamically unstable. The effective diffusivity D^{eff} is negative in this region, cf. Eqs. (45) and (47). An initially homogeneous mixture quenched to lie within this region will undergo spontaneous phase separation by the process of spinodal decomposition. However, Eq. (45) does not account for a surface energy term in the free energy expression.

The remedy is to assume that the free energy of mixing of the system ΔG_{mix} depends both on the composition at a point ϕ_{A} as well as on the composition gradient $\nabla\phi_{\text{A}}$

$$\Delta G_{\text{mix}} = \int_V \left[g_{\text{mix}} + \frac{\kappa}{2}(\nabla\phi_{\text{A}})^2 \right] \mathrm{d}V \tag{48}$$

where κ is the gradient energy parameter that is related to the surface tension σ. Equilibrium is achieved when the above integral is minimized subject to the material balance constraint, i.e.,

$$\overline{\phi_{\text{A}}} = \frac{1}{V}\int_V \phi_{\text{A}}\, \mathrm{d}V \tag{49}$$

where $\overline{\phi_{\text{A}}}$ is the mean concentration of species A. Let us consider $\overline{\phi_{\text{A}}}$ within the two-phase region and the system governed by Eq. (48). Then phase separation would lower the free energy through the g_{mix} term but would necessarily cause a gradient, which would raise the free energy through the κ term. A consequence of this trade-off between bulk and surface energies is that very small systems will not bifurcate into two phases but will remain in the single phase.

Eq. (48) suggests that the gradient of composition be introduced into the generalized definition of chemical potential

$$\mu_{\text{A}} = g_{\text{mix}} - \frac{\kappa}{2}(\nabla\phi_{\text{A}})^2 + (1-\phi_{\text{A}})(g'_{\text{mix}} - \kappa\nabla^2\phi_{\text{A}}) \tag{50}$$

The local balance equation (45) can then be reformulated with the generalized (or gradient-dependent) chemical potential defined by Eq. (50) into

$$\begin{aligned}\frac{\partial\phi_{\text{A}}}{\partial \text{t}} &= \nabla\cdot\left[D\,\frac{\phi_{\text{A}}}{RT}\nabla\left(g_{\text{mix}} - \frac{\kappa}{2}(\nabla\phi_{\text{A}})^2 + (1+\phi_{\text{A}})(g'_{\text{mix}} - \kappa\nabla^2\phi_{\text{A}}) \right) \right] \\ &= \nabla\cdot D\,\frac{\phi_{\text{A}}(1-\phi_{\text{A}})}{RT}(g''_{\text{mix}}\nabla\phi_{\text{A}} - \kappa\nabla^3\phi_{\text{A}})\end{aligned} \tag{51}$$

Spinodal decomposition simulated with Eq. (51) does not generate stationary equilibrium configurations. Instead, it gives non-equilibrium structures that continue to evolve in time even in the late stages of the simulation. There are two mechanisms for domain growth in such quiescent systems. The first is Ostwald ripening, where diffusion of individual molecules through the continuous phase will grow large domains at the expense of smaller ones. The second mechanism is coalescence induced by Brownian motion or convection.

The concept of spinodal decomposition can be extended to multicomponent systems and allow the prediction of various morphologies, e.g., core-shell particles, dual-continuous phases, dual-dispersed phase, and more complex structures. Spinodal decomposition simulations, in contrast to cellular automata, do

not require adjustable constants to predict non-equilibrium morphologies in binary and ternary polymer systems.

6. *Deposition and Dissolution in Porous Media*

One of the important transformation processes in the porous media is the deposition of solid material in pores and the subsequent clogging of the fluid flow through the porous medium. Typical examples are filtration and clogging of well walls in oil fields due to the particles present in the injected fluid. Another example is the deposition of clusters of active catalyst species in porous supports.

Salles *et al.* (1993) modeled the flowing fluid through the porous medium coupled with the deposition of solid particles resulting in the modification of the geometry of the pore space and of the flow through the medium. The velocity field is determined by solving the Stokes equations (26) in the current state of the pore space. The deposition rates are calculated by means of random walks, i.e., the trajectories of individual particles are governed by the convection of the fluid and by the Brownian diffusion. Each time a particle hits a solid wall, it is assumed to stick there, and the amount of such particles is recorded for every elementary area of the solid–liquid interface, i.e., for every face of elementary voxel lying on this interface. Whenever the cumulative quantity of matter deposited on the faces of a given voxel reaches a prescribed threshold, this voxel is converted to solid.

Control of the deposition of Pd films in porous alumina under supercritical CO_2 conditions was investigated by Gummalla *et al.* (2004). Their model captures transport of reactants through the network of capillary pores, homogeneous reaction of reagents producing an intermediate species, nucleation, and growth of the film as a moving boundary problem. The nucleation is treated stochastically at the finest level, whereas transport and reaction at coarser levels are treated deterministically.

In the petroleum industry, HCl is routinely injected into carbonate formations in order to improve oil or gas production. It is known that the porous medium is not etched uniformly by the reactive fluid but that unstable dissolution patterns consisting of highly ramified, empty channels are formed. The channels are commonly called ''wormholes.'' As soon as a wormhole pattern develops, all the fluid will flow through it. Any local increase in the flow rate results in an increase in the local dissolution rate. A piece of porous medium in which a wormhole pattern has been created can be considered as composed of two parts: the first part (wormholes) of very large permeability, and the second part keeping its original permeability.

Daccord *et al.* (1993a, b) investigated systematically the types of patterns that develop by the etching of the porous medium, when the flow rate and the reaction rate (i.e., rate of dissolution) are varied. When the kinetics of the surface reaction is limited, the porous medium is etched in a uniform way on

the microscopic scale, and there is a reaction front of macroscopic size. Mass-transport-limited kinetics creates empty channels (wormholes), which bypass most of the porous medium. For low flow rates, all the dissolution takes place at the entrance of the pores of the medium, and compact patterns are observed.

C. Chemically Reactive Systems

The heterogeneous reactors with supported porous catalysts are one of the driving forces of experimental research and simulations of chemically reactive systems in porous media. It is believed that the combination of theoretical methods and surface science approaches can shorten the time required for the development of a new catalyst and optimization of reaction conditions (Keil, 1996). The multiscale picture of heterogeneous catalytic processes has to be considered, with hydrodynamics and heat transfer playing an important role on the reactor (macro-)scale, significant mass transport resistances on the catalyst particle (meso-)scale and with reaction events restricted within the (micro-)scale on nanometer and sub-nanometer level (Lakatos, 2001; Mann, 1993; Tian *et al.*, 2004).

When modeling phenomena within porous catalyst particles, one has to describe a number of simultaneous processes: (i) multicomponent diffusion of reactants into and out of the pores of the catalyst support, (ii) adsorption of reactants on and desorption of products from catalytic/support surfaces, and (iii) catalytic reaction. A fundamental understanding of catalytic reactions, i.e., cleavage and formation of chemical bonds, can only be achieved with the aid of quantum mechanics and statistical physics. An important subproblem is the description of the porous structure of the support and its optimization with respect to minimum diffusion resistances leading to a higher catalyst performance. Another important subproblem is the nanoscale description of the nature of surfaces, surface phase transitions, and change of the bonds of adsorbed species.

Reaction-transport processes in heterogeneous reactors involve spatial scales in the range from 10^{-9} to 10 m. Here, we are going to survey simulation approaches employed on the scales of nanometers to millimeters.

1. Monte Carlo and Molecular Dynamics Methods

Owing to the large number of molecules in a typical catalyst particle, the sampling to a limited region of the configuration space has to be employed in order to allow computational feasibility. A typical algorithm utilizing the MC approach is the Metropolis algorithm, which generates a random walk in the configurational space (e.g., Allen and Tildesley, 1988). Let us suppose that we

have N molecules in a given configuration confined in a cubic box. Then the following steps are performed iteratively:

(i) a molecule is randomly chosen;
(ii) a trial move is attempted and the molecule is thus displaced and rotated, so that a new set of coordinates is generated from the old one;
(iii) the change in energy of the system A_E due to the trial move is calculated. If the energy A_E has decreased, the move is accepted. If the energy A_E has increased, the move is accepted with the probability $\exp(-A_E/kT)$, where k is the Boltzmann constant and T is the temperature of the system.

For the computation of dynamic properties in physical systems with a high degree of freedom, MD is the most widely used approach. MD calculates the motion of an ensemble of atoms and molecules by integrating Newton's equations. From the motion of the ensemble of atoms and molecules, both microscopic and macroscopic information can be extracted, e.g., transport coefficients, phase diagrams, and structural properties. The physics of the model is contained in a potential energy function for the system, from which the force equations for each atom and molecule are derived. The evaluation of the total force acting on the atom or molecule is the time-consuming step of MD simulations because it requires the computation of a wide range of expressions consisting of terms with fractional powers or transcendental functions, and because the summation of binary force interactions with the neighboring molecules confined in a spherical cutoff of properly chosen radius has to be carried out.

Monte Carlo methods allow the simulation of the reaction kinetics on nanometer-sized (1–100 nm) metal or metal-oxide crystallites deposited on the surface of a porous support (McLeod and Gladden, 1998). The complexity of such systems in combination with relatively high reactant pressures used in the industry hinders the application of results obtained with surface science microscopy and spectroscopy methods (Jansen *et al.*, 2001; Wolff *et al.*, 2003). The complex factors inherent to nanometer chemistry are the reactant supply via the surface diffusion, interplay of reaction kinetics on different facets of crystallites due to the inter-facet diffusion, different rates of reactions on different types of facets, oscillation, and chaos on the nanometer scale (van Neer and Bliek, 1999; Zhdanov, 2002). MC simulations allow one to investigate the kinetics of chemically induced Ostwald ripening on facets of nanometer catalyst particles. Another important effect associated uniquely with small catalyst crystallites on a support is the spill-over effect, consisting generally of adsorption on the support followed by diffusion from the support to the catalyst crystallite or vice versa. The size of the smallest pores in pellets or washcoat varies from 1–2 to $\geqslant 50$ nm. The size of metal crystallites may vary over a very wide range as well. For example, Pt and Rh particles of car exhaust cleaning catalysts are typically 10–100 nm large after some time of use.

Zhdanov and Kasemo (2000) considered the reaction $2A + B_2 \rightarrow 2AB$ occurring via the standard Langmuir–Hinshelwood (LH) mechanism,

$$A_{gas} \rightleftharpoons A_{ads} \tag{52}$$

$$(B_2)_{gas} \rightarrow 2B_{ads} \tag{53}$$

$$A_{ads} + B_{ads} \rightarrow (AB)_{gas} \tag{54}$$

This scheme mimics, e.g., CO or H_2 oxidation on the noble metal catalysts Pt, Pd, or Rh, where symbol A stands for CO or H, and B_2 for O_2. The reaction was simulated on a 2D lattice of adsorption sites. To compare the rates of diffusion and reaction, it is useful to employ the Arrhenius form to represent the rate constants of diffusion jumps of A and B particles to nearest-neighbor vacant sites and for the reaction between two nearest-neighbor reactants, respectively. The diffusion of A is usually rapid when compared to the LH step, while the rate constant for the LH step might be higher, close to, or lower than that for the diffusion of B_2. The MC algorithm used to simulate the $A + B_2$ reaction is as follows:

1. A site on the catalyst surface is selected at random. If the site is vacant, adsorption is attempted (item (2)). If the adsorption trial is successful, the newly adsorbed molecule tries to react (item (3)).
2. A molecule for adsorption is chosen to be A with the probability p and B_2 with the probability $1-p$, where $p \leqslant 1$ is the parameter characterizing the relative impingement rates of A and B_2. To realize adsorption of B_2, a configuration for B_2 is selected at random. An adsorption trial is considered to be successful provided that all the sites of the selected configuration are vacant and belong to the catalyst. Adsorption of the chosen molecule A is realized with the unit probability.
3. For reaction, all the molecules that neighbor the newly adsorbed molecule are identified and one of them is chosen to react.

The size of the crystallites affects the selectivity of reactions with larger molecules, e.g., hydrocarbon chains. Small islands of sites inhibit the adsorption of larger molecules, because all adsorption sites for the selected configuration of the larger molecule have to be vacant. As a general rule, catalytic reactions are structure-sensitive on the scale < 10 nm (Piccolo *et al.*, 1999).

A lattice-gas model of the NO + CO/Pt(1 0 0) reaction was found by Makeev and Kevrekidis (2004) to exhibit bistability and kinetic oscillations. In this simulation, the catalyst surface was represented by a square lattice with periodic boundary conditions. The model includes both chemical reactions and transitions of adsorbed reactants from the nearest-neighbor sites, which are in the

context of the MC simulation described by transition probabilities. The macroscopic simulations of the reactor or catalyst particle can be coupled with microscopic simulations over relatively small ''patches'' of the macroscopic computational domain, which could thus provide an approximation of reaction terms in macroscopic equations.

Lombardo and Bell (1991) reviewed stochastic models of the description of rate processes on the catalyst surface, such as adsorption, diffusion, desorption, and surface reaction, which make it possible to account for surface structure of crystallites, spatial inhomogeneities, and local fluctuations of concentrations. Comparison of dynamic MC and mean-field (effective) description of the problem of diffusion and reaction in zeolites has been made by Coppens *et al.* (1999). Gracia and Wolf (2004) present results of recent MC simulations of CO oxidation on Pt-supported catalysts.

2. *Reaction in Fractal Porous Media*

Fractals are self-similar objects, e.g., Koch curve, Menger sponge, or Devil's staircase. The self-similarity of fractal objects is exact at every spatial scale of their construction (e.g., Avnir, 1989). Mathematically constructed fractal porous media, e.g., the Devil's staircase, can approximate the structures of metallic catalysts, which are considered to be disordered compact aggregates composed of imperfect crystallites with broken faces, steps, and kinks (Mougin *et al.*, 1996).

In the fractal porous medium, the diffusion is anomalous because the molecules are considerably hindered in their movements, cf. e.g., Andrade *et al.*, 1997. For example, Knudsen diffusion depends on the size of the molecule and on the adsorption fractal dimension of the catalyst surface. One way to study the anomalous diffusion is the random walk approach (Coppens and Malek, 2003). The mean square displacement of the random walker $\langle R^2 \rangle$ is not proportional to the diffusion time t, but rather scales in an anomalous way:

$$\lim_{t \to \infty} \langle R^2 \rangle \sim t^{2/D_w} \tag{55}$$

where the dimension of the walk D_w is generally greater than 2. The anomalous scaling law Eq. (55) implies that the classical Brownian or Gaussian diffusion law is no longer valid in fractal media because the fractal substrate induces large-scale correlations on the molecular movement. Consequently, Fick's law is also invalid in its classical form.

Coppens and Froment (1995a, b) employed a fractal pore model of supported catalyst and derived expressions for the pore tortuosity and accessible pore surface area. In the domain of mass transport limitation, the fractal catalyst is more active than a catalyst of smooth uniform pores having similar average properties. Because the Knudsen diffusivity increases with molecular size and decreases with molecular mass, the gas diffusivities of individual species in

multicomponent mixtures will mostly be closer to each other than predicted by the classical expression. It is generally impossible to construct an equivalent, smooth cylindrical pore that leads to the same concentration and flux profiles as those obtained for a fractal pore (Coppens and Froment, 1995a, b). Even when the concentration or pressure profiles in a cylindrical pore are similar to those in the fractal pores, the amounts reacted or produced are usually predicted erroneously by classical Euclidean models. For example, in the fractal pore, up to 7.1 times more vinyl acetate is predicted to be produced on a Pd/Al_2O_3 catalyst than in the smooth pore (Coppens and Froment, 1994).

The selectivity and deactivation processes in pore fractals such as the Sierpinski gasket were simulated by Gavrilov and Sheintuch (1997) and Sheintuch (1999). Their studies investigated, e.g., the effect of the fractal pore structure on the selectivity of a system that incorporates two parallel reactions. Geometrical factors, which influence dynamic processes in a porous fractal solid media, were also investigated by Garza-López and Kozak (1999).

3. *Reaction-transport Models in Reconstructed Porous Media*

After the spatially 2D or 3D model of the porous catalyst support and the distribution of catalyst are generated, the multicomponent diffusion, adsorption, and chemical reaction within this porous structure can be modeled.

Rieckmann and Keil (1997) introduced a model of a 3D network of interconnected cylindrical pores with predefined distribution of pore radii and connectivity and with a volume fraction of pores equal to the porosity. The pore size distribution can be estimated from experimental characteristics obtained, e.g., from nitrogen sorption or mercury porosimetry measurements. Local heterogeneities, e.g., spatial variation in the mean pore size, or the non-uniform distribution of catalytic active centers may be taken into account in pore-network models. In each individual pore of a cylindrical or general shape, the spatially 1D reaction-transport model is formulated, and the continuity equations are formulated at the nodes (i.e., connections of cylindrical capillaries) of the pore space. The transport in each individual pore is governed by the Maxwell–Stefan multicomponent diffusion and convection model. Any common type of reaction kinetics taking place at the pore wall can be implemented.

A similar model has been applied to the modeling of porous media with condensation in the pores. Capillary condensation in the pores of the catalyst in hydroprocessing reactors operated close to the dew point leads to a decrease of conversion at the particle center owing to the loss of surface area available for vapor-phase reaction, and to the liquid-filled pores that contribute less to the flux of reactants (Wood *et al.*, 2002b). Significant changes in catalyst performance thus occur when reactions are accompanied by capillary condensation. A pore-network model incorporates reaction–diffusion processes and the pore filling by capillary condensation. The multicomponent bulk and Knudsen diffusion of vapors in each pore is represented by the Maxwell–Stefan model.

Moreover, the convection of the vapors in the pores was considered and the condensation in the pores was described by the multicomponent Kelvin equation (Shapiro and Stenby, 1977).

Two levels of intraparticle mass transport resistance are considered in various grain or multigrain models, e.g., diffusion resistance in the macro- and micropores in the particle of the highly porous char during its combustion (Cai and Zygourakis, 2004) and monomer transport resistance in macro-pores and polymer micro-grains in the growing polyolefin particle (Debling and Ray, 1995; Kosek *et al*., 2001a).

The techniques of meso-scopic modeling were also applied in the development of the reaction–diffusion model for the hydration and setting of cement (Tzschichholz *et al*., 1996). At the initial stage, the cement particles or powder (e.g., tricalcium silicate, Ca_3SiO_5) are mixed with water. Rapidly after mixing, the dissolution and the reaction of the cement particles starts; the principal reaction products are Ca^{2+}, OH^-, and $H_2SiO_4^{2-}$ ions, which diffuse into water. However, for a given temperature the ion concentrations are bounded by finite solubility products above which solid phases start to precipitate from the solution. There are two precipitation reactions: (i) of calcium hydro-silicate (the so-called ''cement gel''), and (ii) of calcium hydroxide or ''Portlandite.'' While the growth of the cement gel is the basis for the whole cement binding process, the growth of Portlandite mainly happens in order to compensate for the accumulation of Ca^{2+} and OH^- ions in the solution. Tzschichholz *et al*. (1996) proposed a simple stochastic cellular automation model for cement-hydration setting to simulate the spatial and temporal evolution of precipitated microstructures starting from initial random configurations of anhydrous cement particles. The model considers the spatial distribution of solid and liquid phases. The three main chemical reactions (dissolution, precipitation of cement gel, and Portlandite) are coupled with the transport of ions owing to the diffusion.

IV. Applications

A. Multi-scale Reconstruction of a Catalyst Pellet

Experimentally determined effective transport properties of porous bodies, e.g., effective diffusivity and permeability, can be compared with the respective effective transport properties of reconstructed porous media. Such a comparison was found to be satisfactory in the case of sandstones or other materials with relatively narrow pore size distribution (Békri *et al*., 1995; Liang *et al*., 2000b; Yeong and Torquato, 1998b). Critical verification studies of effective transport properties estimated by the concept of reconstructed porous media for porous catalysts with a broad pore size distribution and similar materials are scarce (Mourzenko *et al*., 2001). Let us employ the sample of the porous

alumina with bimodal pore size distribution for such a comparative study; cf. the intrusion mercury porosimetry data of the sample in Fig. 14.

The effective diffusivity and permeability of the porous alumina sample G1 were measured in the Graham diffusion cell and in the permeation cell (Salejova *et al.*, 2004), cf. Table 1. The porosity ε is separated into macro-porosity $\varepsilon_{\text{macro}}$ corresponding to large pores and nano-porosity $\varepsilon_{\text{nano}}$ corresponding to small pores, and $\varepsilon = \varepsilon_{\text{macro}} + \varepsilon_{\text{nano}}$. The boundary in the classification between macro- and nano-pores is somewhat arbitrary selected as the inflection point on the integral mercury porosimetry curve in Fig. 14.

The pellets of porous alumina sample G1 were fractured by the application of the mechanical force, and the bare granular surface of the fracture was examined by SEM; cf. Fig. 15 displaying the granular morphology on the level of hundred micrometers and showing the sub-micrometer morphology. The grain size distribution was evaluated from several SEM images (with the scaling bar 100 μm) as a necessary input for the reconstruction of the spatially 3D porous

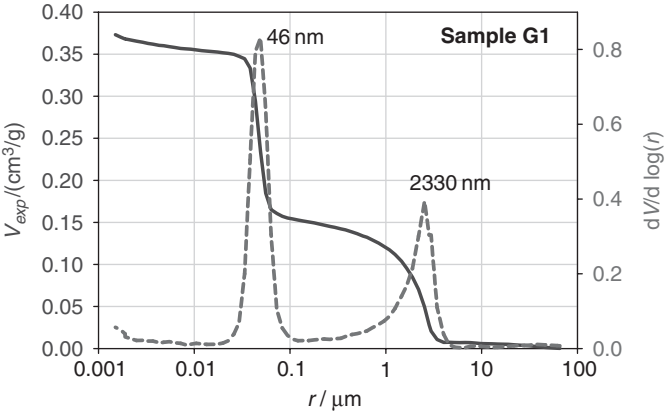

FIG. 14. Integral and differential intrusion mercury porosimetry data for sample G1 (from Salejova *et al.*, 2004).

TABLE 1
TEXTURAL ANALYSIS AND EFFECTIVE TRANSPORT PROPERTIES OF SAMPLE G1

Property	Value
Porosity ε	0.580
Macro-porosity $\varepsilon_{\text{macro}}$	0.235
Nano-porosity $\varepsilon_{\text{nano}}$	0.345
Graham cell results, $\psi = \varepsilon/\tau$	0.199
Permeation cell results, $\langle r\rangle\psi$	277 nm
Permeation cell results, $\langle r^2\rangle\psi$	421,000 nm^2
Permeation cell results $(\langle r\rangle\psi)^2$, $\psi = (\langle r\rangle\psi^2)/(\langle r^2\rangle\psi)$	0.182

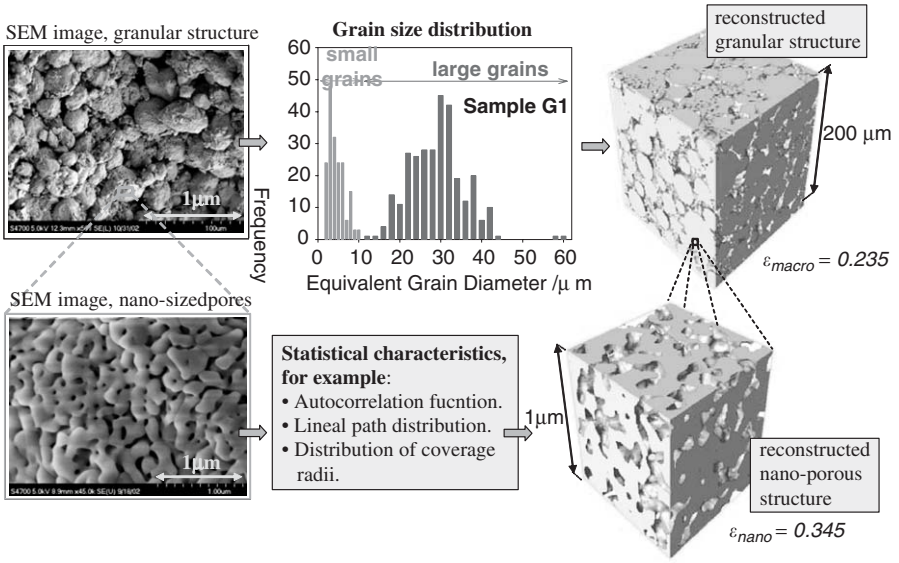

FIG. 15. Reconstruction of multiscale porous media, sample G1 (from Salejova *et al.*, 2004).

structure. The equivalent grain diameter is the diameter of the circle with the same area as that of the grain identified in the image.

The reconstruction algorithm of the granular media places spheres with diameters corresponding to the grain size distribution (from Fig. 15) into a rectangular box, where two pairs of opposite walls are subjected to periodic boundary conditions. The aspect ratio of the height to the width of the rectangular box is 10:1. Because the required target value of porosity of granular media is $\varepsilon_{\text{macro}} = 0.235$, the individual grains are allowed to partially overlap. The newly generated sphere is inserted at the lowest position z_2 in the z-direction, satisfying the equation

$$(r_1 + r_2)(1 - p_{\text{overlap}}) = \sqrt{(x_1 - x_2)^2 + (y_1 - y_2)^2 + (z_1 - z_2)^2} \qquad (56)$$

where (x_1, y_1, z_1) is the coordinate of the center of already placed sphere, (x_2, y_2, z_2) the coordinate of the center of the newly inserted sphere, and r_1 and r_2 the sphere radii of the placed and newly inserted sphere, respectively. The reconstructed sample is thus the list of (x, y, z, r) coordinates of sphere centers and radii. Once the tall rectangular box is filled with spherical grains, its lower half is removed to avoid the effect of regular configuration of spherical grains at the bottom. The cube is selected from the remaining upper part of the rectangular box and is discretized into $101 \times 101 \times 101$ or $201 \times 201 \times 201$ voxels.

The pore structure of the investigated sample G1 on the sub-micron level (with the porosity $\varepsilon_{\text{nano}} = 0.345$) is approximated by the Gaussian-correlated

random field; cf. Fig. 15. The correlation length L_y in Eq. (18) was selected as the modal value of the mercury porosimetry, $L_y = 46\,\text{nm}$; cf. Fig. 14.

The ratio of effective and bulk diffusivity D^{eff}/D is calculated in two steps. First, the effective diffusivity of the nano-porous material with the porosity $\varepsilon_{\text{nano}} = 0.345$ is calculated by the algorithm introduced in Section II.E.1. The effective diffusivity of the nano-porous cube with the size $1\,\mu\text{m}$ and porosity $\varepsilon_{\text{nano}} = 0.345$ displayed in Fig. 15 is $\psi_{\text{nano}} = D^{\text{eff}}/D = (0.112 \pm 0.004)$.

Then, the effective diffusivity of the macro-porous granular material is evaluated. The transport is again governed by the Fick's equation (23), but diffusion also takes place in the "solid phase," which formally represents the nano-porous material, cf. Fig. 15. The diffusion coefficient in the "solid phase" is $D^{\text{solid}} = \psi_{\text{nano}} D = 0.112D$, where D is the bulk diffusivity. The concentration field in the macro-porous media is the solution of Eq. (23) with a diffusivity

$$D = \begin{cases} 1 & \text{in macro-porous phase} \\ 0.112 (= \psi_{\text{nano}}) & \text{in solid phase} \end{cases} \tag{57}$$

The boundary condition of zero accumulation on the interface between macro-pores and "solid phase" is imposed. The effective diffusivity of the porous sample G1 with bimodal pore size distribution is summarized in Fig. 16, where the sample macro-porosity $\varepsilon_{\text{macro}}$ is varied on the horizontal axis. This effective diffusivity is compared with a situation where the diffusion transport in nano-pores is omitted. The contribution of the transport through the nano-porous solid phase to the total diffusion flux is significant. The calculated effective

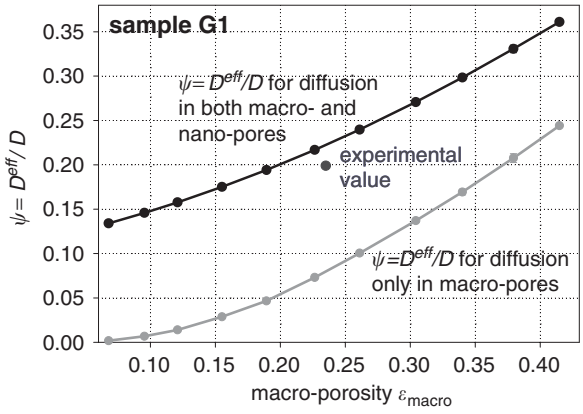

FIG. 16. Effective diffusivity of the examined porous sample G1 calculated for: (i) Fick's diffusion both in macro- and nano-pores, and (ii) Fick's diffusion in macro-pores only. The experimental value of $\psi = D^{\text{eff}}/D = 0.199$ was determined in Grahams diffusion cell. Only grains larger than $10\,\mu\text{m}$ were used in the reconstruction of macro-porous media (from Salejova *et al.*, 2004).

diffusivity is approximately about 10% higher than that determined experimentally in the Graham diffusion cell (Salejova *et al.*, 2004).

The pressure-gradient-driven permeation through nano-pores is considered to be negligible owing to their small characteristic diameter. Therefore, the Darcy's permeability κ_0 was calculated only in the macro-porous reconstructed media. The predicted Darcy's permeability κ_0 is $\sim$3 times larger than the experimental value measured in the permeation cell. This discrepancy is caused by the difficulty of determining the fraction of small grains ($<10\,\mu m$) in the real sample, the assumption of perfectly spherical grains, and by neglecting the effect of the clogged pores (Salejova *et al.*, 2004).

B. Reconstruction of Closed-cell Polymer Foam Structure

This work was motivated by the need to quantify the pentane vapor diffusion through closed-cell polystyrene foam (Salejova *et al.*, 2005). Once the polystyrene foam is formed, the pentane as the blowing agent has to diffuse out from the cellular microstructure and is replaced by air. Freshly foamed polystyrene is not dimensionally stable and it shrinks as it relaxes on the timescale of days to weeks. Environmental concerns call for the reduced consumption of pentane as the blowing agent.

Three-dimensional foam structures can be generated by Voronoi tessellation of sites located on random or regular (e.g., cubic or hexagonal) lattices (Bowyer, 1981). The Voronoi polyhedron is the region of space around a site such that each point of this region is closer to the site than to any other point of the system. A simulated annealing algorithm in connection with Voronoi tessellation can be used to produce a replica of the foam with cell-size distribution corresponding to that of an experimentally processed image of the foam structure. The foam structure can then be reduced to an equivalent network of conductors on which the steady-state diffusion problem is solved and the effective diffusivity determined.

The 3D structure of a foam sample can be obtained by X-ray micro-tomography (Elmoutaouakkil *et al.*, 2002) or it can be reconstructed from a series of 2D images (Garcia-Gonzales *et al.*, 1999). The former technique has been used recently for the structural characterization of PVC foams by means of cell volume distribution, cell coordination number, wall thickness distribution, and total porosity (Elmoutaouakkil *et al.*, 2003). It is also possible to generate foam structures computationally as 3D Voronoi tessellations (Lee, 1999). This was done, e.g., by Kraynik *et al.* (2003), who studied the structure of foams generated by random close packing of monodisperse spheres. Finally, foam structures can be generated by computer simulation of the foaming process. Models of the key steps of bubble nucleation and coarsening (Hilgenfeldt *et al.*, 2001a,b), bubble growth (Koopmans *et al.*, 2000), and foam expansion (Joshi *et al.*, 1998; Körner *et al.*, 2002) have been implemented.

The Voronoi tessellation has been constructed by the following algorithm (Lee, 1999), and its purpose is to generate the 3D structure of high-porosity foams in a computational unit cell consisting of $N_x \times N_y \times N_z$ voxels. The algorithm starts from N_p sites distributed in the unit cell either randomly or at random perturbations of regular lattice positions for two types of lattices—a cubic lattice and a hexagonal lattice. Then, a distance map (''watershed'') is generated by finding the Euclidean distance from each voxel in the unit cell to the nearest site. A Voronoi region around site j is defined as a set V_j of points i such that their Euclidean distance from site j is less than from any other site $k \neq j$, i.e.,

$$V_j = \{i : \ ||\boldsymbol{x}_j - \boldsymbol{x}_i|| < ||\boldsymbol{x}_k - \boldsymbol{x}_i|| \ \forall k \neq j\} \tag{58}$$

The Voronoi regions correspond to cells in a computer-generated foam structure. Examples of cellular structures generated by Voronoi tessellation are shown in Fig. 17.

The volume of cells is calculated as the number of voxels i belonging to each Voronoi region V_j, times the voxel volume h^3, where h is voxel size. The symbol

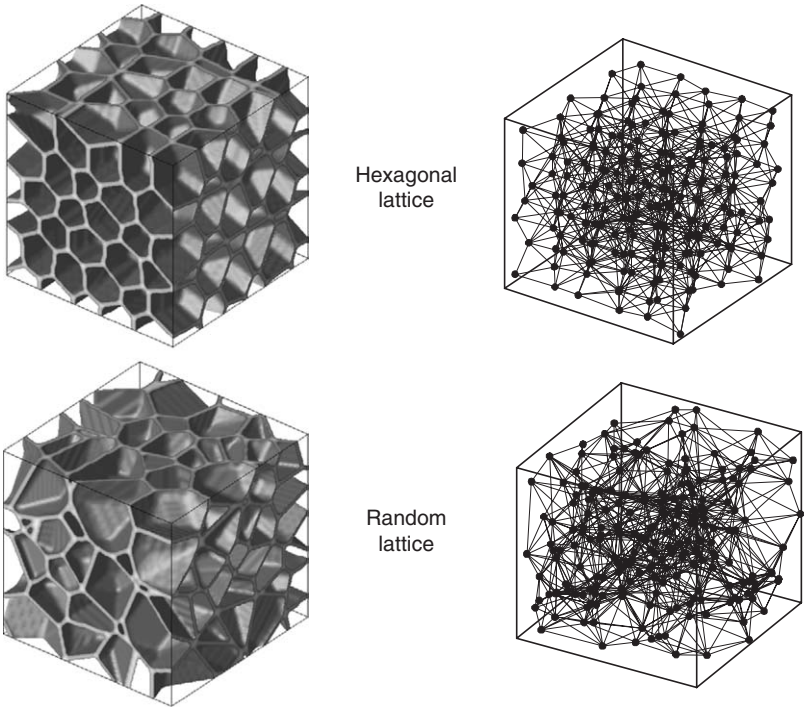

FIG. 17. Computer generated structure of hexagonal and random closed-cell foam obtained by Voronoi tessellation, shown as voxel representation of phase function (left), and network diagram where nodes correspond to cells and bonds to cell walls (from Salejova *et al.*, 2005).

V_j will hereafter also be used to denote the volume of the Voronoi region V_j. A wall dividing two adjacent Voronoi regions is a set of points having an equal distance to the two Voronoi sites. In the discretized voxel space, however, we define a wall A_{jk} as a set of voxels, which belong to Voronoi region V_j and have at least one out of six nearest neighbors in region V_k. The area of the wall cannot be calculated simply as the sum of points in A_{jk} times h^2 because a significant discretization error would be introduced. The area per voxel must be corrected by taking into account the orientation of the wall (the voxel will account for an area equal to h^2 only if the wall is perpendicular to one of the principal coordinate axes). Let n be the number of nearest neighbors of a voxel in a wall A_{jk} that belong to the adjacent Voronoi region V_k. The maximum number of such nearest neighbors is 3. The contribution of each voxel to the total area is weighted by h^2 if $n = 1$, $h^2\sqrt{2}$ if $n = 2$, and $h^2\sqrt{3}/2$ if $n = 3$. The weights are derived from the PLIC (piecewise linear interface construction) scheme often used in simulations of free interface flows by the VOF method (Rider and Kothe, 1998). The symbol A_{jk} will hereafter also be used to denote the area of the wall A_{jk}.

Once the Voronoi tessellation is completed and the areas of the walls dividing adjacent cells in the foam structure are known, the equivalent conductor network can be constructed. The network is a Delaunay triangulation dual to the Voronoi diagram (examples of networks are shown in Fig. 17). Its vortices are the N_p sites used for the construction of the Voronoi diagram and its edges (bonds) link sites that are adjacent in the Voronoi diagram. The structure of the network can be encoded by the connectivity matrix $\boldsymbol{R}$, which is an $N_p \times N_p$ symmetric matrix whose elements are $r_{jk} = r_{kj} = D_s A_{jk}/d_w$ if sites j and k are adjacent, and $r_{jk} = r_{kj} = 0$ otherwise (this includes diagonal elements). The conductivity of the bond

$$r_{jk} = D_s \frac{A_{jk}}{d_w} \tag{59}$$

follows from steady-state diffusion across a planar wall of area A_{jk}, thickness d_w, and diffusion coefficient D_s, assuming Fick's law. The wall thickness d_w is assumed uniform for all walls within the foam. For high-porosity foams, the mean wall thickness d_w and foam porosity ε can be related by the expression

$$\varepsilon = 1 - d_w \frac{a}{2} = 1 - d_w \frac{1}{2} \frac{A_{tot}}{V_{tot}} \tag{60}$$

where $a = A_{tot}/V_{tot}$ is the internal surface area of the foam per unit volume (the factor $\frac{1}{2}$ must be included because each wall contributes twice to the internal surface area). On the computational unit cell, $V_{tot} = N_x N_y N_z h^3$ and $A_{tot} = \sum_{j=1}^{N_p} \sum_{k=1}^{N_p} A_{jk}$.

C. Polymer Particle Morphogenesis

The growth of porous polyolefin particles from supported catalysts can be divided into two main stages (Estenoz and Chiovetta, 2001). In the first stage, the porous-catalyst-support particle with diameter $\approx 20\,\mu m$ is gradually destroyed into fragments of 10–50 nm size owing to the production of polymer in the confined pore space. Porous silica or $MgCl_2$ often serves as a catalyst carrier. The outcome of the first stage is the set of fragments embedded in the continuous but porous matrix of polymer phase (Kakugo *et al.*, 1989). At the beginning of the second stage of particle growth, most of the catalyst carrier has already been fragmented, and the growth and morphogenesis of porous polyolefin particles then continues owing to the polymerization at active catalyst sites immobilized typically at the surface of fragments of catalyst carrier (Debling and Ray, 2001). The typical final size of porous polyolefin particles is 0.5–2 mm.

Let us first consider the catalyst/polyolefin particle in the early stage of its evolution. The particle consists of the solid catalyst carrier with catalyst sites immobilized on its surface, polymer phase, and pores. The first-principle-based meso-scopic model of particle evolution has to be capable of describing the formation of polymer at catalyst sites, transport of monomer(s) and other reactants/diluents through the polymer and pore space, and deformation of the polymer and catalyst carrier (including its fragmentation). Similar discrete element modeling techniques have been applied previously to different problems (Heyes *et al.*, 2004; Mikami *et al.*, 1998; Tsuji *et al.*, 1993).

Let us discretize the catalyst carrier, the polymer phase, and the void phase into a number of small, spherical micro-elements of several types with elastic or viscoelastic interactions acting among individual micro-elements, and with transport processes taking place along the connections of neighboring micro-elements; cf. Fig. 18. The catalyst carrier is thus represented by microelements C, but microelements with catalyst sites immobilized on their surface are denoted by C^*. All catalyst sites are assumed to have constant activity for demonstration purposes in this chapter. One growing polymer micro-element P^* is attached to each "catalyst" micro-element C^*. When the radius of the growing polymer micro-element P^* reaches a prescribed value, it becomes the non-growing polymer microelement P, and a new microelement of type P^* is formed at catalyst center C^*. The pores are discretized into void-phase micro-elements V in order to describe the transport of reactants/diluents in pores. For the sake of simplicity, we consider only the transport and reaction of monomer and not of other reactants.

The ith micro-element is characterized by the position of its center x_i, velocity $\boldsymbol{v}_i$, radius r_i, monomer concentration c_i, and by its type t_i. The translational movement of each micro-element is governed by kinematic equation and Newton's equation of momentum

$$\frac{\mathrm{d}\boldsymbol{x}_i}{\mathrm{d}t} = \boldsymbol{v}_i, \quad t_i = \mathrm{C}, \mathrm{C}^*, \mathrm{P}, \mathrm{P}^*, \mathrm{V} \tag{61}$$

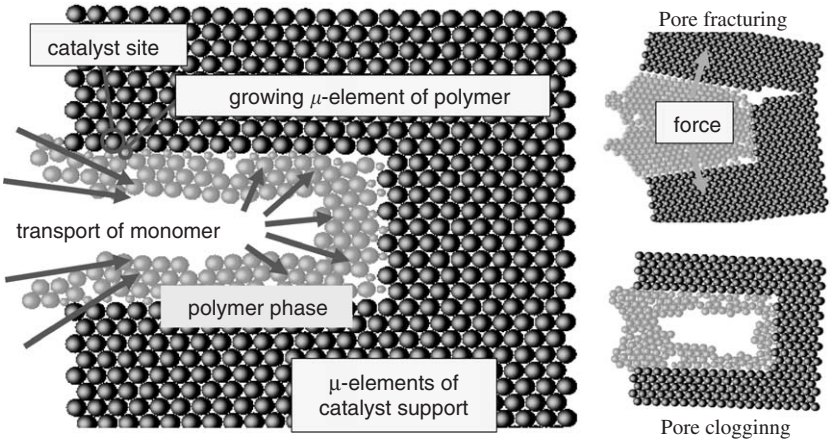

FIG. 18. Model of the fragmentation of catalyst support based on force interactions and transport among micro-elements of five types: (i) catalyst support, (ii) catalyst support with active catalyst site, (iii) growing polymer micro-element, (iv) non-growing polymer microelement, and (v) void-space transport micro-element (from Grof *et al.*, 2005c).

$$\frac{\mathrm{d}(m_i \boldsymbol{v}_i)}{\mathrm{d}t} = \sum_j \boldsymbol{F}_{ij}^{\text{binary}} + \sum_{j,k} \boldsymbol{F}_{ijk}^{\text{ternary}}, \quad t_i = \mathrm{C}, \mathrm{C}^*, \mathrm{P}, \mathrm{P}^*$$
$$\boldsymbol{v}_i = \boldsymbol{0}, \quad t_i = \mathrm{V} \tag{62}$$

where $m_i = \frac{4}{3}\pi\rho_i r_i^3$ is the mass of the ith micro-element, and the density of each micro-element ρ_i is considered to be constant in time. Summations of forces $\boldsymbol{F}$ on the right-hand side of Eq. (62) are carried out over all binary and ternary interactions between the ith micro-element and its connected neighbors. The positions of pore-phase micro-elements V are fixed during the simulation.

The balance of the monomer in the ith micro-element is

$$\frac{\mathrm{d}}{\mathrm{d}t}(c_i V_i) = \sum_j N_{ij} - S_i, \quad t_i = \mathrm{P}, \mathrm{P}^*, \mathrm{V}$$
$$c_i = 0, \quad t_i = \mathrm{C}, \mathrm{C}^* \tag{63}$$

where $V_i = \frac{4}{3}\pi r_i^3$ is the volume of the ith micro-element, N_{ij} the molar flux of monomer from the jth connected micro-element, and S_i the rate of monomer consumption by the reaction. No monomer is assumed to be present inside the catalyst-support micro-elements C and C*.

The rate of the growth of the ith micro-element of type P^* depends on the monomer concentration in this micro-element

$$\frac{\mathrm{d}m_i}{\mathrm{d}t} = 4\pi\rho_i r_i^2 \frac{\mathrm{d}r_i}{\mathrm{d}t} = k m_{\mathrm{cat},j} c_i, \quad t_i = \mathrm{P}^*$$
$$\frac{\mathrm{d}r_i}{\mathrm{d}t} = 0, \quad t_i = \mathrm{C}, \mathrm{C}^*, \mathrm{P}, \mathrm{V} \tag{64}$$

where $m_{\mathrm{cat},j}$ is the mass of catalyst in the micro-element C_j^* to which the ith micro-element P_i^* is attached. Let A_Y be the polymer yield rate at reactor bulk temperature in $\mathrm{kg_{pol}/g_{cat}}h$. Then the rate constant $k = A_\mathrm{Y}/(3.6c_\mathrm{eq})$, where $c_\mathrm{eq} = Hc_\mathrm{bulk}$ is the concentration of monomer in micro-elements P^*, which is in equilibrium with the bulk concentration of monomer in the reactor c_bulk; and H is the equilibrium constant. The rate of monomer consumption in Eq. (63) is evaluated as

$$S_i = \begin{cases} (k m_{\mathrm{cat},j} c_i)/M_\mathrm{M}, & t_i = \mathrm{P}^* \\ 0 & t_i = \mathrm{P}, \mathrm{V} \end{cases} \tag{65}$$

where M_M is the molecular weight of the monomer.

The mathematical model of catalyst/polymer particle evolution consists of the set of differential-algebraic equations (61)–(64). The constitutive equations describing the force interactions, transport of monomer, phase equilibria at the interface between polymer and pore phase as well as the rules for connectivity of micro-elements have to be specified (Grof and Kosek, 2005; Grof *et al.*, 2005a).

1. Force Interactions between Micro-Elements

Magnitudes of binary and ternary force interactions required in Eq. (62) are calculated by simple elastic or visco-elastic constitutive equations and then projected into force vectors. Elastic model is the direct implementation of the Hook's law with the stress between micro-elements A and B dependent linearly on the strain e_AB:

$$F_\mathrm{AB}/A_\mathrm{AB} = E^t e_\mathrm{AB} \tag{66}$$

where E^t is the elastic modulus dependent on the type of connected microelements, A_AB the contact area, and F_AB the binary interaction force. The positive value of F_AB results in the attraction and the negative one in the repulsion of micro-elements. The strain e_AB is defined as

$$e_\mathrm{AB} = (|\boldsymbol{u}| - u_0)/u_0 \tag{67}$$

where $u_0 = r_\mathrm{A} + r_\mathrm{B}$ is the equilibrium distance and $\boldsymbol{u} = \boldsymbol{x}_\mathrm{B} - \boldsymbol{x}_\mathrm{A}$ the vector connecting micro-elements A and B.

Ternary interactions are considered in the case of the deformation of the triplet of the connected micro-elements A–V–B. If the translation of microelements leads to the change of the angle $\alpha = \angle\mathrm{AVB}$, then the force with the magnitude F_α acts on micro-elements as the resistance against this change. The magnitude of the force F_α is calculated in the limit of elastic interactions as

$$F_\alpha / A_{\mathrm{AB}} = -G^t(\cos\alpha - \cos\alpha_0) \tag{68}$$

where G^t is the bending modulus specific to the type of connected microelements, and α_0 the original value of the angle $\angle$AVB at the start of the simulation (or at the time when the triplet A–V–B was formed). The contact area A_{AB} is, for the sake of simplicity, selected for both the binary and ternary interactions as $A_{\mathrm{AB}} = \frac{1}{2}\pi(r_{\mathrm{A}}^2 + r_{\mathrm{B}}^2)$, although for the ternary interaction, the micro-elements A and B do not have to be in the direct contact.

The visco-elastic interactions of connected micro-elements of semicrystalline polyolefins are approximated by the Maxwell model, which formally consists of the spring with modulus E^t and the viscous dashpot characterized by the viscosity η^t connected in series,

$$\frac{\mathrm{d}\sigma}{\mathrm{d}t} = E^t \frac{\mathrm{d}e_{\mathrm{AB}}}{\mathrm{d}t} - \frac{E^t\sigma}{\eta^t} \tag{69}$$

where $\sigma = F_{\mathrm{AB}}/A_{\mathrm{AB}}$ is the stress. The Maxwell model describes particularly well the relaxation of stress in a visco-elastic material. When the connection of micro-elements A and B is subjected to constant strain ($\mathrm{d}e_{\mathrm{AB}}/\mathrm{d}t = 0$), then the stress in the connection decays exponentially, i.e., $\sigma = \sigma_0 \exp(-E^t t/\eta^t) = \sigma_0 \exp(-t/\tau_{\mathrm{R}}^t)$, where σ_0 is the initial stress at $t = 0$ and $r_{\mathrm{R}}^t = \eta^t/E^t$ the relaxation time. The Maxwell model also allows for permanent deformation.

The magnitudes of force interactions F_{AB} and F_α defined by constitutive Equations (66), (68), and (69) have to be projected into vectors required in Eq. (62); cf. Grof *et al.* (2005a).

Force interactions among micro-elements were calculated in our simulations according to the following rules:

- $F_{AB} = 0$ and $F_\alpha = 0$, if at least one of the connected micro-elements is of the type V (i.e., void phase).
- The Maxwell model Eq. (69) is employed to calculate the magnitude of the binary force interaction if both micro-elements are of the type P or P*.
- Elastic model given by Eq. (66) with different moduli for the attractive and for the repulsive forces is used to calculate the magnitude of the binary interaction F_{AB} in the remaining cases, i.e., in the cases involving at least one catalyst micro-element C or C*.
- All ternary interactions involving micro-elements of type C, C*, P, and P* are considered to be elastic and are calculated according to Eq. (68).

2. Connectivity of Micro-Elements

For the purpose of calculation of force interactions, the computational algorithm keeps the list of connected pairs of neighboring micro-elements and the list of connected triplets of micro-elements. These lists are updated, i.e., new connections are created or existing connections are removed at each step of dynamic simulation. Let us describe the rules for the creation and deletion of bonds of micro-elements.

Micro-elements A and B become connected when they touch each other, i.e., when their distance $u = |\boldsymbol{u}|$ becomes

$$|\boldsymbol{u}| \leqslant u_0 = r_A + r_B \tag{70}$$

Two elements become disconnected if the strain between them exceeds maximum value $e^t_{\max}$

$$e_{AB} = \frac{|\boldsymbol{u}| - u_0}{u_0} > e^t_{\max} \tag{71}$$

The value of the maximum strain $e^t_{\max}$ depends on the type of micro-elements A and B. Thus the superscript "t" in the previous equation can be (a) "PP," to denote the connection between two polymer micro-elements P or P*; (b) "CC," to denote the connection between two catalyst micro-elements C or C*; and, finally, (c) "PC," to denote the connection between polymer and catalyst micro-elements.

The triplet A–V–B is initiated when both connections A–V and B–V are formed. For the sake of simplicity and in order to reduce the number of triplets that have to be processed, the connections A–V and B–V have to be of the same type, i.e., of the type "PP," "CC," or "PC." The triplet is deleted if (i) one of the connections A–V or B–V is disconnected, or (ii) the deviation between the actual angle α and the initial angle α_0 exceeds the limiting value $\alpha^t_{\max}$, i.e. $|\alpha - \alpha_0| > \alpha^t_{\max}$ (and in this case also, one of the binary connections A–V and B–V is disconnected).

Once the catalyst breaks, it remains broken even if the fragmented parts come into contact later during the simulation. On the other hand, the polymer micro-elements P or P* are assumed to be "sticky," and connections between them created during the simulation are assumed to be as strong as the connections at the beginning of the simulation.

3. Diffusion Transport of the Monomer

The molar flux of monomer N_{ij} from the jth into the ith micro-element is described as

$$N_{ij} = D^t_{ij}(c_j - c_i)\frac{A_{ij}}{\delta_{ij}} \tag{72}$$

where the area is $A_{ij} = \frac{1}{2}\pi(r_i^2 + r_j^2)$ and $\delta_{ij} = |\boldsymbol{x}_i - \boldsymbol{x}_j|$ is the distance between the micro-elements. Diffusion coefficients in the void phase D_{V} and in the polymer phase D_{P} are different; hence, the diffusivity D_{ij}^t depends on the type of connected micro-element

$$D_{ij}^t = \begin{cases} 0 & t_i = \mathrm{C}, \mathrm{C}^* \text{ or } t_j = \mathrm{C}, \mathrm{C}^* \\ D_{\mathrm{P}} & t_i = \mathrm{P}, \mathrm{P}^* \text{ or } t_j = \mathrm{P}, \mathrm{P}^* \\ D_{\mathrm{V}} & t_i = \mathrm{V} \text{ and } t_j = \mathrm{V} \\ D_{\mathrm{PV}}, & (t_i = \mathrm{V} \text{ and } t_j = \mathrm{P}, \mathrm{P}^*) \text{ or vice versa} \end{cases} \tag{73}$$

No monomer transport through the solid catalyst support is considered. The diffusivity D_{PV} in Eq. (73) is only a formal notation because the flux between the void phase V and the polymer P (or P*) micro-elements is calculated from the assumption of no accumulation and sorption equilibrium at the phase interface.

The void-phase micro-elements V are used to model the transport of monomer through the regions where neither polymer nor catalyst micro-elements are present. The micro-elements V do not change their position or radius during the dynamic simulation, but they are deleted when the catalyst or the polymer micro-elements move over them and are inserted as needed to cover any newly formed void phase. The transport connections between the micro-elements are different from the connections with the force interactions described in Sections IV.C.1 and IV.C.2, and are also regularly updated during the dynamic simulation.

4. Evolution of Particle Morphology

The simultaneous evolution of the catalyst support, the polymer phase, and the concentration field of the monomer is displayed in the sequence of images in Fig. 19. The catalyst carrier is only partially covered by the catalyst. The evolution of micro-elements is driven by the force interactions and by the growth of polymer micro-elements P*, and is coupled with the transport of monomer through the dynamically evolving void and polymer phases. The produced polymer phase contains a number of cavities because the simulation is spatially 2D; hence, the coordination number of polymer microelements is lower than in 3D simulations. The initial and the final configurations of the simple catalyst/polymer particle is shown in Fig. 20. The discrete element modeling of catalyst particle fragmentation allows one to address a number of practical problems of catalytic polymerization of olefins, e.g., the dependence of the incorporation of a co-monomer on the pore space characteristics of catalyst support, the dependence of fragmentation and particle growth on the impregnation of the porous support by the catalyst system, the discrimination between the "shrinking core" and the "gradual bi-section" fragmentation modes of catalyst support, etc. (Kittilsen and McKenna, 2001; Knoke *et al.*, 2003; Pater *et al.*, 2003).

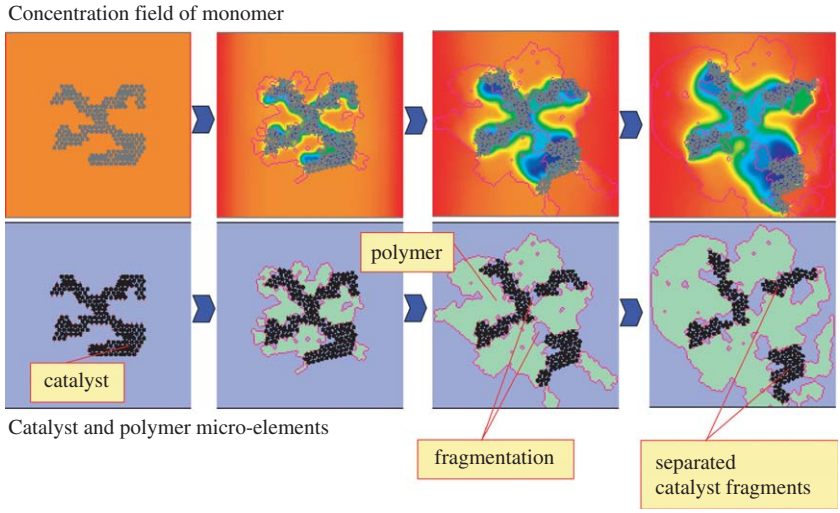

FIG. 19. Fragmentation of a simple catalyst carrier during early stages of catalytic polymerization of olefins. The upper row of pictures represents the concentration field of monomer (red = high, blue = low concentration), the lower row of pictures represents the evolution of particle morphology (from Grof *et al.*, 2005c).

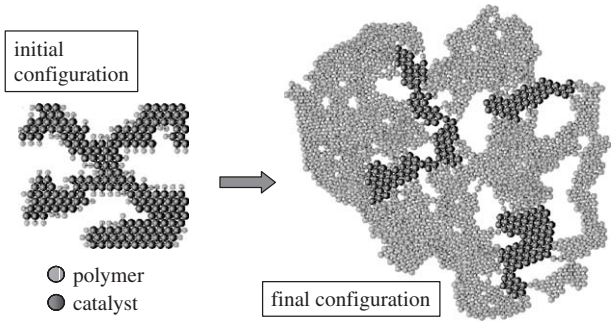

FIG. 20. Detail of the initial and the final configuration of the growing catalyst/polymer particle from Fig. 19. The polymer phase in the final configuration contains large number of voids because of the smaller number of connections in spatially 2D simulation when compared to spatially 3D case (from Grof *et al.*, 2005c).

Alternatively, we can consider the model of the growing particle consisting only of a single type of the growing micro-element (Grof *et al.*, 2005a); cf. Fig. 21. In this case, the dynamic simulation starts from a hypothetical initial condition just after the fragmentation of the catalyst carrier, and thus describes the second stage of particle growth. The predictive capabilities of this model were demonstrated in important problems of the formation of fine particles and the particles with macro-cavities in dependence on reaction conditions. We have

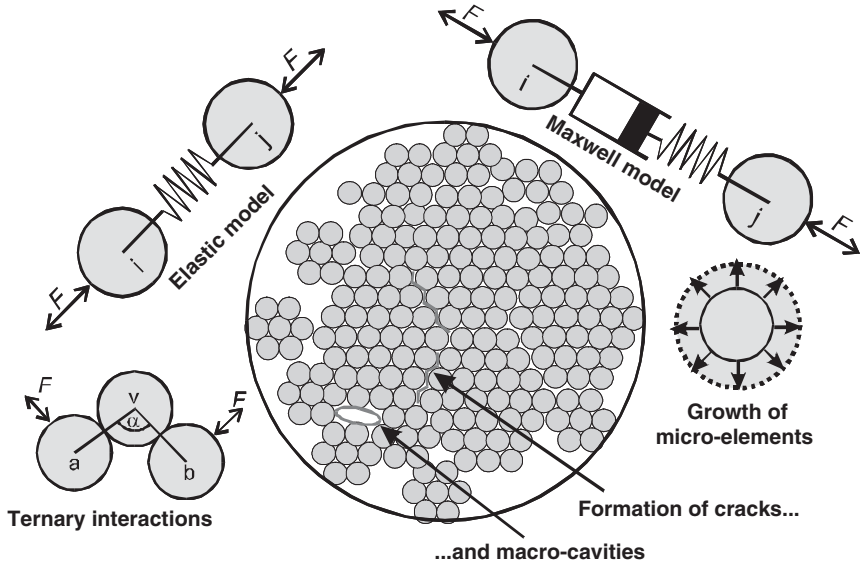

FIG. 21. Morphogenesis model of porous polyolefin particle based on the elastic and visco-elastic interactions among micro-elements (from Grof *et al.*, 2005a).

also demonstrated the non-perfect replication of particle shape during its growth even in the case of an initially uniform distribution of catalyst activity in the particle (Grof *et al.*, 2005b). The importance of the distribution of catalyst in individual micro-elements just after the fragmentation was stressed, and its effect on the final morphology of polyolefin particle was demonstrated. Thus, a mapping from the distribution of catalyst in fragments as a result of the first stage of particle evolution into the final morphology of polyolefin particle was demonstrated, and the importance of the first "fragmentation" stage of particle evolution on its final morphology observed experimentally has been confirmed. The effect of the relaxation time τ_R in the Maxwell model Eq. (69) on the predicted morphology of polyolefin particle is illustrated in Fig. 22. In this figure, the simulation started from a uniform distribution of micro-elements, and the diffusion resistance in the growing particle was considered.

D. Granulation and Dissolution

Many chemical products, such as pigments, fertilizers, detergents, pharmaceuticals, or food and beverage products, are in the form of granules, i.e., agglomerates of primary particles held together by a binder. The microstructure of the agglomerate, i.e., the distribution of individual components, binder, and porosity within the granule, has a significant influence on its end-use properties, such as rate of dissolution. The granule design problem consists of finding a

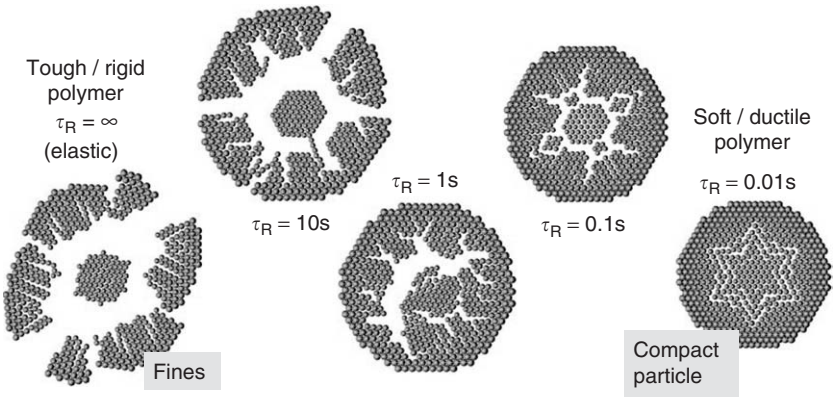

FIG. 22. Evolution of particle morphology in dependence on the relaxation time τ_R of the Maxwell model. Lower (higher) polymerization temperature corresponds to longer (shorter) relaxation time τ_R. The initial condition of the simulation was a perfectly regular circle of uniformly distributed micro-elements. The growth of micro-elements in the particle center is slower because of monomer diffusion limitation (from Grof *et al.*, 2005a).

microstructure that leads to a specified dissolution rate for a given formulation (i.e., chemical composition of the granule), and establishing processing routes and conditions that will lead to the formation of that microstructure.

The problem of granule microstructure formation in the specific case of low-shear, wet-granulation processes (e.g., fluid bed, drum, or pan granulation) has been considered by Stepanek and Ansari (2005). They have described a method for constructing "virtual granules" by explicit simulation of primary particle packing, binder spreading, and binder solidification. A single virtual granule is built in a unit cell by sequential deposition of solid primary particles and liquid-binder droplets, as illustrated in Fig. 23. A range of granule microstructures can then be generated by varying the primary particle properties (size distribution and morphology), the binder/solids ratio, the binder spreading rate (through viscosity and dynamic contact angle), and the binder solidification rate. Stepanek and Ansari (2005) have systematically investigated the effect of these parameters on granule microstructure, and generated structure maps relating granule porosity to the characteristic times of the deposition, spreading, and solidification processes.

Once the virtual granules have been created, it is of interest to relate their microstructure to the dissolution rate and release profile of an active component. Recently, Stepanek (2004) carried out detailed simulations of virtual granules. The problem of porous media dissolution is encountered not only during the application of pharmaceutical or detergent granules and tablets but also in industrial processes such as leaching (Erlebacher *et al.*, 2001) or extraction (Adrover *et al.*, 2004), as well as in other engineering applications such as

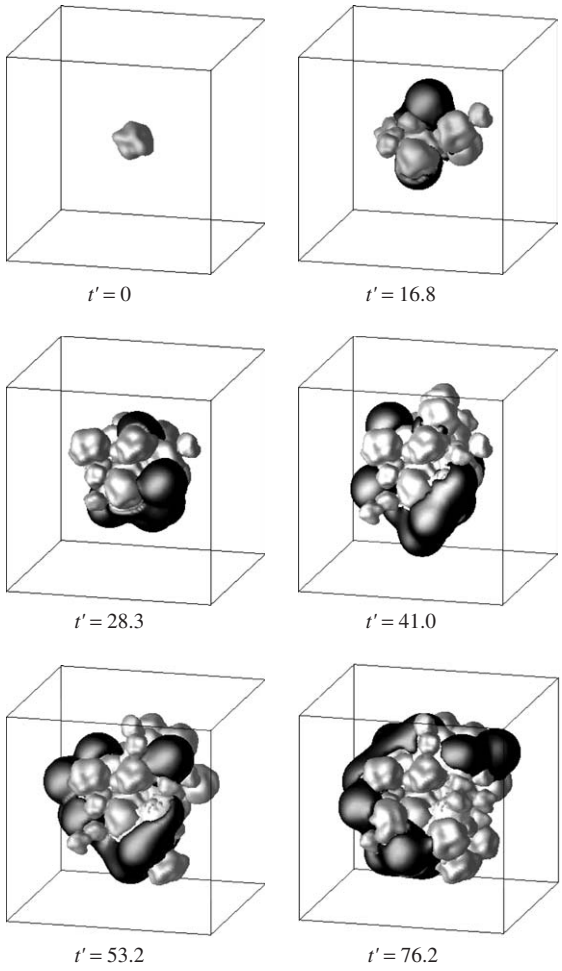

FIG. 23. Sequential deposition of primary solid particles and liquid binder droplets leading to the formation of a virtual granule (from Stepanek and Ansari, 2005).

oil recovery (Békri *et al.*, 1995). Dissolution can be formally regarded as a morphology transformation operation, i.e., an operation affecting the phase functions $f_i(\boldsymbol{r})$ defined in Section II.A. The morphology transformation is due to the dissolution of soluble phases at the solid–liquid interface. The dissolution can be purely physical or accompanied by a heterogeneous or homogeneous chemical reaction, coupled with diffusion-only or convection–diffusion transport of the dissolved species. (Combustion can be regarded as a gas-phase analogy of dissolution and will not be discussed here separately.)

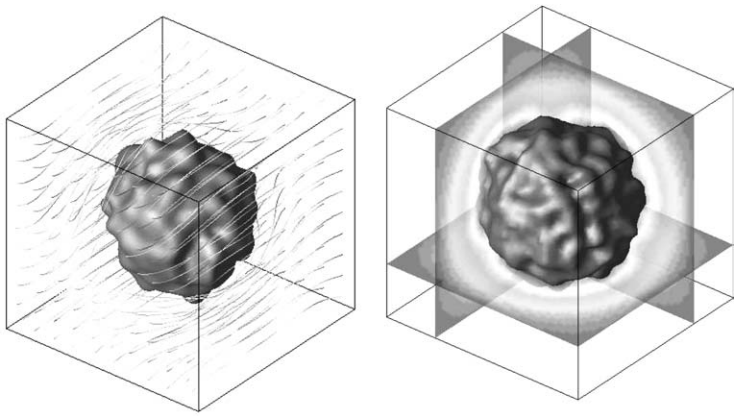

FIG. 24. Velocity (left) and concentration (right) profiles during the simulation of granule dissolution (from Stepanek, 2004).

The simulation of the dissolution of a multicomponent porous medium (including virtual granules) can be summarized into the following steps:

1. Start from an initial structure—defined by phase functions $f_i(\boldsymbol{r}, t = 0)$.
2. Solve a convection–diffusion problem in the fluid phase surrounding (granules) or penetrating (porous media) the object of interest.
3. Update phase functions according to local dissolution rates.
4. Check the connectivity of the solid skeleton—remove disconnected solid phase if present.
5. Repeat from Step 2 until the end time is reached.

This methodology has been used by Békri *et al.* (1995) for the simulation of porous media dissolution, and recently by Stepanek (2004) for the studying of the dissolution and breakup of agglomerates; cf. Fig. 24. He has constructed structure-dissolution maps for two-component porous agglomerates and obtained correlations for the dissolution half-time t_{50} as function of granule composition (binder/solids ratio, porosity), ingredient properties (solubility and diffusivity of binder and primary solids), and hydrodynamic regime (dissolution under stagnant and flow conditions).

E. Simulation of CO Oxidation on Reconstructed Catalytic Washcoat

The effective-scale models have been most often used in the description of transport and reaction processes within the porous structure of catalysts. Such models are based on the introduction of an effective diffusion coefficient D_e, that is used in the analogy to the Fick's law for the description of diffusion

fluxes in the porous medium (Satterfield, 1980; Schmidt, 1998). The classical approach to studies of diffusion and reaction in porous catalysts uses the models of cylindrical pores. Recent re-examination of the pore diffusion problem was made by Balakotaiah and Gupta (2000). Discussion of recent approaches to mesoscopic modeling of diffusion–reaction through a microporous medium is contained in the recent paper by Chatterjee *et al.* (2004). Microkinetic modeling based on mean field theory has been reviewed by Dumesic *et al.* (1992). Post-treatments of zeolite-supported catalysts in order to modify their activity and stability were discussed by Abdullah *et al.* (2004) and illustrated on TEM images of actual micropore structures.

The catalytic washcoat of the monolith converters of automotive exhaust gas usually consists of partly sintered γ-Al_2O_3 particles of different sizes that together form a (macro-)porous layer. The γ-Al_2O_3 particles themselves are also porous, with pore sizes belonging to the range of meso-pores (diameter $\sim$10 nm). Crystallites of noble metals (typically Pt) are dispersed on the γ-Al_2O_3 support as active catalytic components. Other components, e.g., CeO_2-ZrO_2, are added to the washcoat for the stabilization of the porous structure; they may also act as active catalytic centers (Koci *et al.*, 2004a). Catalytic reactions take place on the Pt sites located in the meso-pores of γ-Al_2O_3 simultaneously with the transport of gaseous reaction components. The transport inside the meso-porous γ-Al_2O_3 particles is characterized by the effective diffusivity based on Knudsen diffusion, while the transport in the macro-pores can be described by volume diffusion (Koci *et al.*, 2004b).

SEM and TEM images give detailed information about the porous structure of a supported heterogeneous catalyst (pore size distribution, typical sizes of the particles, etc.). The information from SEM and TEM images can be used in the reconstruction of porous catalytic medium. In the digitally reconstructed catalyst, transport (diffusion, permeation), adsorption, reaction, and combined reaction–diffusion processes can be simulated (Stepanek *et al.*, 2001a). Parametric studies can be performed, and the resulting dependencies can serve as a feedback for the catalyst development.

The macro-porosity $\varepsilon_{\text{macro}}$ and the correlation function corresponding to the macro-pore size distribution of the washcoat were evaluated from the SEM images of a typical three-way catalytic monolith, cf. Fig. 25. The reconstructed medium is represented by a 3D matrix and exhibits the same porosity and correlation function (distribution of macro-pores) as the original porous catalyst. It contains the information about the phase at each discretization point—either gas (macro-pore) or solid (meso-porous Pt/γ-Al_2O_3 particle). In the first approximation, no difference is made between γ-Al_2O_3 and CeO_2 support, and the catalytic sites of only one type (Pt) are considered with uniform distribution.

In the following example, we use a simple microkinetic model of CO oxidation on Pt together with the reconstructed porous catalyst to follow the evolution of local concentration profiles within the porous structure. The reaction–diffusion problem of the CO oxidation on the Pt/γ-Al_2O_3 porous catalyst

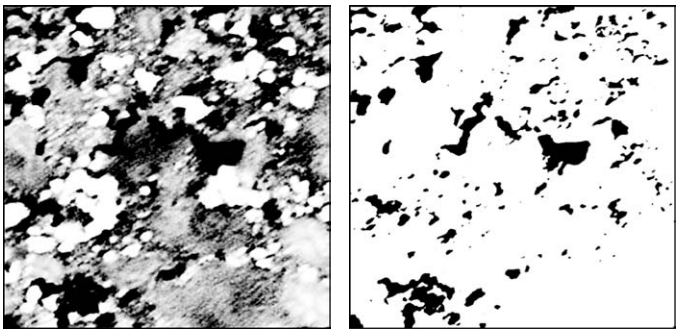

FIG. 25. Typical SEM image of porous Pt/Rh/CeO_2/γ-Al_2O_3 catalytic washcoat (left) and the corresponding binarized image (only the macro-pores visible; right). In the SEM image, the black color corresponds to the macro-pores, the grey color corresponds to the meso-porous γ-Al_2O_3 with dispersed Pt, and the white color corresponds to CeO_2. Length of the section edge is 10 μm. The average macro-porosity evaluated from more SEM images is approx. $\varepsilon_{\text{macro}} = 0.15$ (from Koci *et al.*, 2004).

can be described by the following partial differential equations (spatially 3D distributed problem):

$$\frac{\partial c_k}{\partial t} = D_k^{\text{eff}} \nabla^2 c_k + \sum_j \nu_{kj} \tau_j, \quad k = \text{CO}, \text{O}_2, \text{CO}^*, \text{O}^* \tag{74}$$

Equation (74) were solved within the section of the reconstructed porous catalyst, represented by the 3D matrix. Here x, y, and z are the spatial coordinates in the porous catalyst, c_k denotes the molar concentration of the kth component, D_k^{eff} is the effective diffusivity of the kth component, ν_{kj} is the stoichiometric coefficient of the component k in the jth reaction step, and r_j is the reaction rate of the jth reaction step.

The characteristic length of the washcoat section to be simulated is ~10 μm; thus, we may consider constant temperature profile on this scale. Since the volume diffusion in the macro-pores is much faster than the Knudsen diffusion in the meso-pores of the γ-Al_2O_3 particles, we may further assume that the CO and O_2 gas concentrations in the macro-pores are constant within the simulated washcoat section. For the surface-deposited components CO^* and O^*, a zero diffusivity is used, i.e., $D_k^{\text{eff}} = 0$. For gaseous CO and O_2, the effective diffusivities are based on the Knudsen diffusivity in the meso-pores (with diameter ~10 nm) of the γ-Al_2O_3.

The microkinetics with an explicit consideration of the surface-deposited species has been employed,

$$\begin{aligned}
&\text{CO} + * \leftrightarrow \text{CO}^*, && r_1 = k_1^f C_{\text{Pt}} y_{\text{CO}} \theta_* - k_1^b L_{\text{Pt}} \theta_{\text{CO}^*} \\
&\text{O}_2 + 2* \rightarrow 2\text{O}^*, && r_2 = k_2 C_{\text{Pt}} Y_{\text{O}_2} \theta_* \\
&\text{CO}^* + \text{O}^* \rightarrow \text{CO}_2 + 2*, && r_3 = k_3 C_{\text{Pt}} \theta_{\text{CO}^*} \theta_{\text{O}^*}
\end{aligned}$$

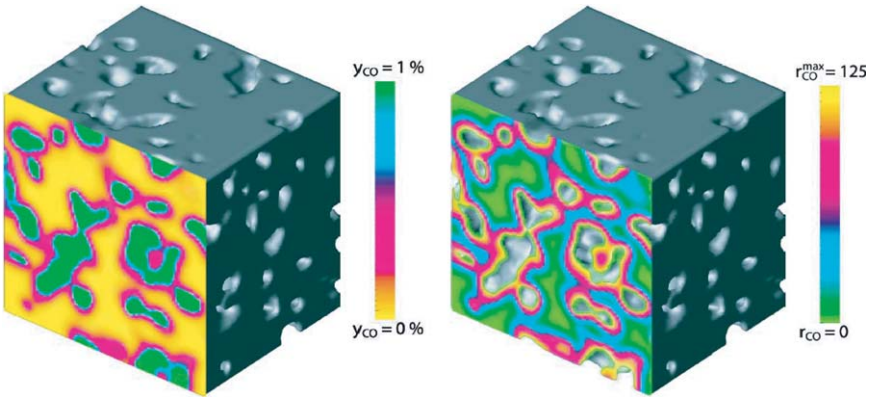

FIG. 26. Profiles of CO concentration y_{CO} and reaction rate r_{CO} in the reconstructed Pt/γ-Al_2O_3 catalyst (cross-section), $T = 300°C$, $L_{xy} = 540\,nm$, $\varepsilon_{macro} = 0.15$, $C_{Pt} = 50\,mol/m^3$, $D^{eff} = 6 \times 10^{-8}\,m^2/s$. Free space corresponds to the macro-pores, solid grey corresponds to meso-porous γ–Al_2O_3 with dispersed Pt. Length of the section edge is 10 μm (from Koci *et al.*, 2004).

Here * denotes the catalytic Pt-site, C_{Pt} the concentration of the catalytic sites, y_k the molar fractions of the gaseous components (CO, O_2), and θ_k the relative surface concentrations of the deposited components (CO^*, O^*). The values of kinetic parameters k_j are taken from Nibbelke *et al.* (1998), where the complete microkinetic scheme for CO oxidation on Pt/Rh/CeO_2/γ-Al_2O_3 catalyst is given. In Fig. 26 we can observe that steep concentration gradients may occur in the system. There are even regions with zero CO concentration inside the sintered γ-Al_2O_3 particles, and the reaction takes place only on the surface of the macro-pores. The Pt distributed deeper is not utilized in the reaction.

The results of the parametric studies (e.g., the influence of noble metal distribution and correlation length) provide a better understanding of the reaction-transport effects in porous, supported heterogeneous catalysts (Bhattacharya *et al.*, 2004). In the combination with semi-deterministic methods of the reconstruction (simulation of the catalyst preparation process), the results can be used for the optimization of the washcoat structure.

V. Outlooks

A. Biological Systems

Plant and animal tissue has a complex microstructure (e.g., Khaled and Vafai, 2003), consisting of cells, extra-cellular matrix (ECM), and porosity. Tissue and other biological systems are usually structured over several length-scales (Chu and Lee, 2004). Convective transport in a tissue is controlled by the vascular

network (Kumar *et al.*, 2004). When describing transport at the length-scale of the network, the tissue surrounding the capillaries is typically treated as an effective medium with volume-averaged properties (Lasseux *et al.*, 2004), which depend on the microstructure—phase volume fraction of ECM, etc. The methods presented in this chapter are applicable with little or no modification to the modeling of transport in complex biological structures and cellular assemblies (Picioreanu *et al.*, 2004; Wood *et al.*, 2002a).

One of the aims of the emerging discipline of *tissue engineering* (Mantalaris, 2001; Mantalaris *et al.*, 2001) is *ex vivo* growth of tissues from cells, including stem cells (Rippon and Bishop, 2004). A typical tissue growth protocol would consist of seeding the cells into a biodegradable porous scaffold, which is then immersed into a cultivation medium containing the required nutrients and signals. The cells would then proliferate in the scaffold and produce their own extracellular matrix that eventually replaces the degradable scaffold as structural support. The resulting tissue must have a specific microstructure in order to posses the same functionality as natural tissue. The microstructure depends on the interplay of initial scaffold morphology, spatial distribution of seed cells, diffusion of nutrients and metabolites in and out of the scaffold, and the cell proliferation and scaffold degradation rates. The methods presented in this chapter are directly applicable to the modeling of morphology transformation processes occurring during tissue growth.

B. Materials Design

The field of synthesis and fabrication of porous materials with controlled pore size and morphology has progressed enormously in recent years. Techniques such as colloidal templating (Linssen *et al.*, 2003; Velev and Lenhoff, 2000; Xia *et al.*, 2000) or directed self-assembly (Lin *et al.*, 2001; Pilleni, 2001; Texter and Tirrell, 2001; Xu and Goedel, 2002) have made it possible to fabricate porous solids with specific microstructures at a wide range of length-scales (Soten and Ozin, 1999). Moreover, the ''bottom–up'' materials synthesis techniques (Shimomura and Sawadaishi, 2001) can be combined with ''top–bottom'' microfabrication methods to form truly multi-scale hybrid structures such as microchannel networks internally coated with templated porous solid (Xu and Platzer, 2001; Yang *et al.*, 2001).

Owing in part to the fabrication techniques mentioned above, it is legitimate to pose the problem of rational design of materials with tailor-made microstructure. As part of the material microstructure design process, the structure-property mapping problem has to be solved—i.e., the problem of calculating a set of end-use properties (e.g., effective transport properties) for a material microstructure described by a given set of integral characteristics (porosity, specific surface area, etc.). The second important element of the material microstructure design process is a solution of the process-structure mapping

problem—i.e., the problem of determining the microstructure that results from a series of morphology-transformation operations (particle packing, sintering, leaching, etc.). A materials synthesis recipe can then be derived from the sequence of morphology-transformation operations.

The modeling methods reviewed in this chapter (i.e., evaluation of integral characteristics, calculation of effective transport properties, and diagenesis-based models of microstructure formation) are directly relevant to the solution of both structure-property and process-structure problems. While the "forward" problems have a unique solution, the inverse problems usually do not. A challenge for material microstructure design is to identify suitable optimization algorithms for the solution of the inverse problems (e.g., Torquato *et al*., 2002). Stochastic optimization algorithms applied at one length-scale (e.g., McLeod and Gladden, 2000) can be combined with deterministic algorithms at a larger length-scale (e.g., Gheorghiu and Coppens, 2004) to optimize multi-scale structures such as heterogeneous catalysts. Similarly, discrete and continuous algorithms may need to be combined in situations where one microstructure parameter, such as phase volume fraction, is inherently continuous, while some other parameter, such as the order in which microstructure transformation operations are applied, is inherently discrete. Analogous problems are of course well known from standard process systems engineering, and inspiration will undoubtedly be found in that field for the solution of material microstructure design problems.

VI. Conclusions

The methodology for digital representation, characterization and reconstruction of porous and multi-phase media has been presented in this chapter. Computational techniques for the determination of effective transport properties (conductivity, diffusivity, permeability, and tensile properties) have been reviewed, as well as methods for the solution of transient reaction, transport, and morphology-transformation processes in those media. The application of the techniques has been demonstrated on several examples: polymer particle growth and morphogenesis, granulation and dissolution, and heterogeneous catalysis. Finally, two emerging application areas of the computational methods have been reviewed, namely, tissue engineering and structured materials design.

We hope to have demonstrated that computer simulation of transport and transformation processes on digitally reconstructed multi-phase media can be beneficial to practical chemical engineering applications. We believe that as chemical engineering becomes more "product-oriented," the need to model phenomena that control material microstructure formation will gain in importance. We hope that this chapter will provide a useful starting point for those who wish to familiarize themselves with the relevant computational techniques.

ACKNOWLEDGMENTS

We thank our colleagues and students Zdeněk Grof, Martin Kohout, Petr Kočí and Gabriela Salejová for their work on preparation of illustrative pictures. JK and MM gratefully acknowledge the support of the Grant Agency of the Czech Republic (project 104/02/0325) and of the Ministry of Education (project MSM 6046137306).

REFERENCES

Abdullah, A. Z., Bakar, M. Z. A., and Bhatia, S. *J. Chem. Technol. and Biotechnol.* **79**, 761–768 (2004).
Adler, P. M., "Porous Media: Geometry and Transports". Butterworth-Heinemann, Boston (1992).
Adler, P. M. *Curr. Top. Phys. Fluids* **1**, 277–306 (1994).
Adler, P. M., and Thovert, J. F. *Appl. Mech. Rev.* **51**(9), 537–585 (1998).
Adrover, A., Velardo, A., Giona, M., Cerbelli, S., Pagnanelli, F., and Toro, L. *Chem. Eng. J.* **99**, 89–104 (2004).
Allen, M. P., and Tildesley, D. J., "Computer Simulation of Liquids". Clarendon Press, New York (1988).
Andrade, J. S., Street, D. A., Shibusa, Y., Havlin, S., and Stanley, H. E. *Phys. Rev. E* **55**, 772–777 (1997).
Arenas-Alatorre, J., Avalos-Borja, M., and Diaz, G. *Appl. Surf. Sci.* **189**, 7–17 (2002).
Argento, C., and Bouvard, D. *Int. J. Heat Mass Trans.* **39**, 1343–1350 (1996).
Aris, R., "The Mathematical Theory of Diffusion and Reaction in Permeable Catalysts". Clarendon Press, Oxford (1975).
Arns, C. H., Knackstedt, M. A., Pinczewski, V. W., and Mecke, K. R. *Phys. Rev. E* **63**, 031112 (2001).
Arns, C. H., Knackstedt, M. A., and Mecke, K. R. *Coll. Surf. A: Physicochem. and Eng. Aspects* **241**, 351–372 (2004).
Atwood, R. C., and Lee, P. D. *Acta Mater.* **51**, 5447–5466 (2003).
Avnir, D., "Fractal Approach to Heterogeneous Chemistry: Surfaces Colloids and Polymers". Wiley, New York (1989).
Balakotaiah, V., and Gupta, N. *Chem. Eng. Sci.* **55**, 3505–3514 (2000).
Barrie, P. J. *Ann. Rep. NMR Spectrosc.* **41**, 265–316 (2000).
Békri, S., Thovert, J. -F., and Adler, P. M. *Chem. Eng. Sci.* **50**, 2765–2791 (1995).
Bell, A. T. *Science* **299**, 1688–1691 (2003).
Bhatia, S. K. *Chem. Eng. Sci.* **41**, 1311–1324 (1986).
Bhattacharya, M., Harold, M. P., and Balakotaiah, V. *Chem. Eng. Sci.* **59**, 3737–3766 (2004).
Blacher, S., Léonard, A., Heinrichs, B., Tcherkassova, N., Ferauche, F., Crine, M., Marchot, P., Loukine, E., and Pirard, J. -P. *Coll. Surf. A: Physicochem. Eng. Aspects* **241**, 201–206 (2004).
Blunt, M. J., Jackson, M. D., Piri, M., and Valvatne, P. H. *Adv. Water Resour.* **25**, 1069–1089 (2002).
Bowyer, A. *Comput. J.* **24**(2), 162–166 (1981).
Cai, Y., and Zygourakis, K. *Ind. Eng. Chem. Res.* **42**, 2746–2755 (2004).
Capek, P., Hejtmánek, V., and Šolcová, O. *Chem. Eng. J.* **81**, 281–285 (2001).
Chatterjee, A., Snyder, M. A., and Vlachos, D. G. *Chem. Eng. Sci.* **59**, 5559–5567 (2004).
Chu, C. P., and Lee, D. J. *Chem. Eng. Sci.* **59**, 1875–1883 (2004).

Coppens, M. -O., and Froment, G. F. *Chem. Eng. Sci.* **49**, 4897–4907 (1994).
Coppens, M. -O., and Froment, G. F. *Chem. Eng. Sci.* **50**, 1013–1026 (1995a).
Coppens, M. -O., and Froment, G. F. *Chem. Eng. Sci.* **50**, 1027–1039 (1995b).
Coppens, M. -O., Bell, A. T., and Chakraborty, A. K. *Chem. Eng. Sci.* **54**, 3455–3463 (1999).
Coppens, M. -O., and Malek, K. *Chem. Eng. Sci.* **58**, 4787–4795 (2003).
Daccord, G., Lenormand, R., and Liétard, O. *Chem. Eng. Sci.* **48**(1), 169–178 (1993a).
Daccord, G., Liétard, O., and Lenormand, R. *Chem. Eng. Sci.* **48**(1), 179–186 (1993b).
Davies, G. M., and Seaton, N. A. *AIChE J.* **46**, 1753–1768 (2000).
Debling, J. A., and Ray, W. H. *Ind. Eng. Chem. Res.* **34**, 3466–3480 (1995).
Debling, J. A., and Ray, W. H. *J. Appl. Polym. Sci.* **81**, 3085–3106 (2001).
Dodds, P. S., and Rothman, D. H. *Annu. Rev. Earth Planet. Sci.* **28**, 571–610 (2000).
Dominquez, A., Bories, S., and Prat, M. *Int. J. Multiphas. Flow* **26**, 1951–1979 (2000).
Dumesic, J. A., Rudd, D. F., Aparicio, L. M., Rekoske, J. E., and Tervino, A. A., ''The Microkinetics of Heterogeneous Catalysis''. American Chemical Society, Washington (1992).
Elmoutaouakkil, A., Fuchs, G., Bergounhon, P., Péres, R., and Peyrin, F. *J. Phys. D: Appl. Phys.* **36**, A37–A43 (2003).
Elmoutaouakkil, A., Salvo, L., Maire, E., and Peix, G. *Adv. Eng. Mater.* **4**, 803–807 (2002).
El-Nafaty, U. A., and Mann, R. *Chem. Eng. Sci.* **56**, 856–872 (2001).
Erlebacher, J., Aziz, M. J., Karma, A., Dimitrov, N., and Sieradzki, K. *Nature* **410**, 450–453 (2001).
Estenoz, D. A., and Chiovetta, M. G. *J. Appl. Polym. Sci.* **81**, 285–311 (2001).
Farber, L., Tardos, G., and Michaels, J. N. *Powder Technol.* **132**, 57–63 (2003).
Feres, R., and Yablonsky, G. *Chem. Eng. Sci.* **59**, 1541–1556 (2004).
Galani, A. N., Kainourgiakis, M. E., Kikkinides, E. S., Steriotis, Th., Stubos, A. K., and Papaioannou, A. *Coll. Surf. A: Physicochem. Eng. Aspects* **241**, 273–279 (2004).
Garcia-Gonzales, R., Monnereau, C., Thovert, J. -F., Adler, P. M., and Vignes-Adler, M. *Coll. Surf. A: Physicochem. Eng. Aspects* **151**, 497–503 (1999).
Garza-López, R. A., and Kozak, J. J. *J. Phys. Chem. B* **103**, 9200–9204 (1999).
Gavrilov, C., and Sheintuch, M. *AIChE J.* **43**, 1691–1699 (1997).
Gheorghiu, S., and Coppens, M. -O. *AIChE J.* **50**, 812–820 (2004).
Giona, M., Adrover, A., and Giona, A. R. *Chem. Eng. Sci.* **50**, 1001–1011 (1995).
Gracia, F. J., and Wolf, E. E. *Chem. Eng. Sci.* **59**, 4723–4729 (2004).
Gregg, S. J., and Sing, K. S. W., ''Adsorption, Surface Area and Porosity''. Academic Press, London (1982).
Grof, Z., Kosek, J., Marek, M., and Adler, P. M. *AIChE J.* **49**(4), 1002–1013 (2003).
Grof, Z., and Kosek, J., 2005. Dynamics of fragmentation of catalyst carriers in catalytic polymerization of olefins. In preparation (2005).
Grof, Z., Kosek, J., and Marek, M. *AIChE J.* **51**(7), 2048–2067 (2005a).
Grof, Z., Kosek, J., and Marek, M. *Ind. Eng. Chem. Res.* **44**, 2389–2404 (2005b).
Groot, R. D., and Warren, P. B. *J. Chem. Phys.* **11**, 4423–4435 (1997).
Gummalla, M., Tsapatsis, M., Watkins, J. J., and Vlachos, D. G. *AIChE J.* **50**, 684–695 (2004).
Gupper, A., Wilhelm, P., Schmied, M., Kazarian, S. G., Chan, K. L. A., and Reußner, J. *Appl. Spectrosc.* **56**, 1515–1523 (2002).
Hazlett, R. D. *Math. Geol.* **29**(6), 801 (1997).
Heyes, D. M., Baxter, J., Tüzün, U., and Qin, R. S. *Philos. Trans. Roy. Soc. London A* **362**, 1853–1865 (2004).
Hilgenfeldt, S., Kraynik, A. M., Koehler, S. A., and Stone, H. A. *Phys. Rev. Lett.* **86**, 2685–2688 (2001a).
Hilgenfeldt, S., Koehler, S. A., and Stone, H. A. *Phys. Rev. Lett.* **86**, 4704–4707 (2001b).
Hoebink, J. H. B. J., and Marin, G. B. Modeling of Monolithic Reactors for Automotive Exhaust Gas Treatment, in A. Cybulski and J. A. Moulijn, ''Structured Catalysts and Reactors''. Marcel Dekker, NY (1998).
Hosier, I. L., Alamo, R. G., and Lin, J. S. *Polymer* **45**, 3441–3455 (2004).

Ingram, G. D., Cameron, I. T., and Hangos, K. M. *Chem. Eng. Sci.* **59**, 2171–2187 (2004).
Ichikawa, S., Akita, T., Okumura, M., Kohyama, M., and Tanaka, K. *JEOL News* **38**, 6–9 (2003).
Jackson, R., "Transport in Porous Catalysts". Elsevier, Amsterdam (1977).
Jansen, W. P. A., Harmsen, J. M. A., Denier, A. W., Hoebink, J. H. B. J., Schouten, J. C., and Brongersma, H. H. *J. Catal.* **204**, 420–427 (2001).
Janssen, A. H., Koster, A. J., and de Jong, K. P. *Angew. Chem. Int. Edit.* **40**, 1102–1104 (2001).
Joshi, K., Lee, J. G., Shafi, M. A., and Flumerfelt, R. W. *J. Appl. Polym. Sci.* **67**, 1353–1368 (1998).
Kainourgiakis, M. E., Steriotis, Th., Kikkinides, E. S., Romanos, G., and Stubos, A. K. *Coll. Surf. A: Physicochem. Eng. Aspects* **206**, 321–334 (2002).
Kakugo, M., Sadatoshi, H., Yokoyama, M., and Kojima, K. *Macromolecules* **22**, 547–551 (1989).
Kanamori, K., Nakanishi, K., Hirao, K., and Jinnai, H. *Coll. Surf. A: Physicochem. Eng. Aspects* **241**, 215–224 (2004).
Keil, F. J. *Chem. Eng. Sci.* **51**, 1543–1568 (1996).
Khaled, A. -R. A., and Vafai, K. *Int. J. Heat Mass Trans.* **46**, 4989–5003 (2003).
Kim, J. C., Auh, K. H., and Martin, D. M. *Model. Simul. Mater. Sci. Eng.* **8**, 159–168 (2000).
Kittilsen, P., and McKenna, T. F. *J. Appl. Polym. Sci.* **82**, 1047–1060 (2001).
Knoke, S., Korber, F., Fink, G., and Tesche, B. *Macromol. Chem. Phys.* **204**(4), 607–617 (2003).
Koci, P., Kubicek, M., and Marek, M. *Chem. Eng. Res. Dev.* **82**, 284 (2004a).
Koci, P., Stepanek, F., Kubicek, K., and Marek, M. Modeling of CO Oxidation in Digitally Reconstructed Porous $Pt/\gamma Al_2O_3$ Catalyst. "Proceedings of CHISA 2004", 22–25 August 2004, Prague, Czech Republic (2004b).
Kohout, M., Collier, A. P., and Stepanek, F. *Int. J. Heat Mass Trans.* **47**, 5565–5574 (2004).
Kohout, M., Collier, A.P., and Stepanek, F. *Powder Technol.*, in press (2005).
Kohout, M., Collier, A.P., and Stepanek, F. Vacuum Contact Drying: Multi-Scale Modeling and Experiments, *in* "European Symposium on Computer Aided Process Engineering – 14" (A. Barbosa-Povoa, and H. Matos Eds.), pp. 1075–1080. Elsevier Science, Amsterdam (2004).
Koopmans, R. J., den Doelder, J. C. F., and Paquet, A. N. *Adv. Mater.* **12**, 1873–1880 (2000).
Körner, C., Thies, M., and Singer, R. F. *Adv. Eng. Mater.* **4**, 765–769 (2002).
Kosek, J., Grof, Z., Novak, A., Stepanek, F., and Marek, M. *Chem. Eng. Sci.* **56**, 3951–3977 (2001a).
Kosek, J., Stepanek, F., Novak, A., Grof, Z., and Marek, M. Multi-Scale Modeling of Growing Polymer Particles in Heterogeneous Catalytic Reactors, *in* "European Symposium on Computer Aided Process Engineering – 11" (R. Gani, S. B. Jorgensen Eds.), pp. 177–182. Elsevier Science, Amsterdam (2001b).
Kothe, D. B., Rider, W. J., Mosso, S. J., Brock, J. S., and Hochstein, J. I. Volume tracking of interfaces having surface tension in two and three dimensions. Technical Report AIAA 96-0859 (1996).
Kraynik, A. M., Reinelt, D. A., and van Swol, F. *Phys. Rev. E* **67**, 031403 (2003).
Krishna, R. *Chem. Eng. Sci.* **48**, 845–861 (1993).
Krishna, R., and Wesseling, J. A. *Chem. Eng. Sci.* **52**(6), 861–911 (1997).
Kumar, R., Stepanek, F., and Mantalaris, A. *Food Bioprod. Process.* **82**, 105–116 (2004).
Lakatos, B. G. *Chem. Eng. Sci.* **56**, 659–666 (2001).
Lasseux, D., Ahmadi, A., Cleis, X., and Garnier, J. *Chem. Eng. Sci.* **59**, 1949–1964 (2004).
Lee, D.T., Computational Geometry II – Proximity, *in* "Algorithm & Theory of Computation Handbook, Chapter 20.2" (M. J. Atallah, Ed.), CRC Press, Boca Raton, USA (1999).
Lee, P. D., Chirazi, A., Atwood, R. D., and Wang, W. *Mater. Sci. Eng. A* **365**, 57–65 (2004).
Li, X., and Yortsos, Y. C. *Chem. Eng. Sci.* **50**, 1247–1271 (1995).
Liang, Z., Ioannidis, M. A., and Chatzis, I. *J. Colloid Interf. Sci.* **221**, 13–24 (2000a).
Liang, Z., Ioannidis, M. A., and Chatzis, I. *Chem. Eng. Sci.* **55**, 5247–5262 (2000b).
Liger-Belair, G., Vignes-Adler, M., Voisin, C., Robillard, B., and Jeandet, P. *Langmuir* **18**, 1294–1301 (2002).
Lin, C. L., and Miller, J. D. *Chem. Eng. J.* **80**, 221–231 (2000).

Lin, X. M., Jaeger, H. M., Sorensen, C. M., and Klabunde, K. J. *J. Phys. Chem. B* **105**, 3353–3357 (2001).
Linssen, T., Cassiers, K., Cool, P., and Vansant, E. F. *Adv. Colloid Interf. Sci.* **103**, 121–147 (2003).
Lombardo, S. J., and Bell, A. T. *Surf. Sci. Rep.* **13**(1–2), 1–72 (1991).
Losic, N., Thovert, J. -F., and Adler, P. M. *J. Colloid Interf. Sci.* **186**, 420–433 (1997).
Ma, M. C., and Sonka, M. *Computer Vision and Image Understanding* **64**(3), 420 (1996).
Makeev, A. G., and Kevrekidis, I. G. *Chem. Eng. Sci.* **59**, 1733–1743 (2004).
Mann, R. *Chem. Eng. Res. Des.* **71**, 551–562 (1993).
Mantalaris, A. *Chem. Eng.* **720**, 32–34 (2001).
Mantalaris, A., Panoskaltsis, N., Sakai, Y., Bourne, P., Chang, C., Messing, E. M., and Wu, J. H. D. *J. Pathol.* **193**, 361–366 (2001).
Manwart, C., Torquato, S., and Hilfer, R. *Phys. Rev. E* **62**, 893–899 (2000).
Martys, N. S., and Garboczi, E. J. *Phys. Rev. B* **46**, 6080–6090 (1992).
Mason, E. A., and Malinauskas, A. P., ''Gas Transport in Porous Media: The Dusty-Gas Model''. Elsevier, Amsterdam (1983).
McLeod, A. S., and Gladden, L. F. *J. Catal.* **173**, 43–52 (1998).
McLeod, A. S., and Gladden, L. F. *J. Chem. Inf. Comp. Sci.* **40**, 981–987 (2000).
Mikami, T., Kamiya, H., and Horio, M. *Chem. Eng. Sci.* **53**(10), 1927–1940 (1998).
Mourzenko, V. V., Thovert, J. -F., and Adler, P. M. *Eur. Phys. J. B* **19**, 75–85 (2001).
Mougin, P., Pons, M., and Villermaux, J. *Chem. Eng. J.* **64**, 63–68 (1996).
Nam, J. H., and Kaviany, M. *Int. J. Heat Mass Trans.* **46**, 4595–4611 (2003).
Nauman, E. B., and He, D. Q. *Chem. Eng. Sci.* **56**, 1999–2018 (2001).
Nibbelke, R. H., Nievergeld, A. J., Hoebink, J. H., and Marin, G. B. *Appl. Catal. B: Environ.* **19**, 245 (1998).
Pater, J. T. M., Weickert, G., and van Swaaij, W. P. M. *J. Appl. Polym. Sci.* **87**, 1421–1435 (2003).
Perré, P. Meshpore: A Software Able to Apply Image-Based Meshing Techniques to Anisotropic and Heterogeneous Porous Media. ''Drying 2004 – Proceedings of the 14th International Drying Symposium'', pp. 664–671, Sao Paulo, Brazil, 22–25 August 2004.
Piccolo, I., Becker, C., and Henry, C. R. *Eur. Phys. J. D* **9**, 415–419 (1999).
Picioreanu, C., Kreft, J. -U., and van Loosdrecht, M. C. M. *Appl. Environ. Microbiol.* **70**, 3024–3040 (2004).
Pilleni, M. P. *J. Phys. Chem. B* **105**, 3358–3371 (2001).
Poulet, J., Manzoni, D., Hage-Chehade, F., Jacquin, C. J., Boutéca, M. J., Thovert, J. -F., and Adler, P. M. *J. Mech. Phys. Solids* **44**(10), 1587–1620 (1996).
Quintard, M., Kaviany, M., and Whitaker, S. *Adv. Water Resour.* **20**, 77–94 (1997).
Ramaswamy, S., Gupta, M., Goel, A., Aaltosalmi, U., Kataja, M., Koponen, A., and Ramarao, B. V. *Coll. Surf. A: Physicochem. Eng. Aspects* **241**, 232–333 (2004).
Rider, W. J., and Kothe, D. B. *J. Comput. Phys.* **141**, 112–152 (1998).
Rieckmann, C., and Keil, F. J. *Ind. Eng. Chem. Res.* **36**, 3275–3281 (1997).
Rigby, S. P., and Daut, S. *Adv. Colloid Interf. Sci.* **98**, 87–119 (2002).
Rippon, H. J., and Bishop, A. E. *Cell Proliferat.* **37**, 23–34 (2004).
Roberts, A. P., and Knackstedt, M. A. *Phys. Rev. E* **54**, 2313–2328 (1996).
Roberts, A. P., and Torquato, S. *Phys. Rev. E* **59**, 4953–4963 (1999).
Rozman, M. G., and Utz, M. *Phys. Rev. E* **63**, 066701 (2001).
Sahimi, M. *Rev. Mod. Phys.* **65**, 1393–1534 (1993).
Sahimi, M., Gavalas, G. R., and Tsotsis, T. T. *Chem. Eng. Sci.* **45**, 1443–1502 (1990).
Sahimi, M., Heidarinasabb, A., and Dabirb, B. *Chem. Eng. Sci.* **59**, 4289–4301 (2004).
Salejova, G., Kosek, J., Nevoral, V., Solcova, O., and Schneider, P. Effective Transport Properties of Reconstructed Porous Catalyst Carriers. ''Proceedings of CHISA 2004'', 22–25 August 2004, Prague, Czech Republic (2004).
Salejova, G., Kosek J., and Stepanek F. Effective diffusivity of random and regular cellular structures. In preparation (2005).

Salles, J., Thovert, J. -F., and Adler, P. M. *Chem. Eng. Sci.* **48**, 2839–2858 (1993).
Sapoval, B., Andrade, J. S., and Filochea, M. *Chem. Eng. Sci.* **56**, 5011–5023 (2001).
Satterfield, Ch. N., "Heterogeneous Catalysis in Practice". McGraw-Hill, New York (1980).
Scardovelli, R., and Zaleski, S. *Annu. Rev. Fluid Mech.* **31**, 567–603 (1999).
Schmidt, L. D., "The Engineering of Chemical Reactions". Oxford University Press, Oxford (1998).
Schneider, P., and Gelbin, D. *Chem. Eng. Sci.* **40**, 1093–1099 (1984).
Sethian, J. A., "Level Set Methods". Cambridge University Press, New York (1996).
Shapiro, A. A., and Stenby, E. H. *Fluid Phase Equilibr.* **134**, 87–101 (1977).
Sheintuch, M. *Ind. Eng. Chem. Res.* **38**, 3261–3269 (1999).
Shimomura, M., and Sawadaishi, T. *Curr. Opin. Colloid Interf. Sci.* **6**, 11–16 (2001).
Silverstein, D. L., and Fort, T. *Langmuir* **16**, 839–844 (2000).
Soten, I., and Ozin, G. A. *Curr. Opin. Colloid Interf. Sci.* **4**, 325–337 (1999).
Stepanek, F. *Chem. Eng. Res. Desig.* **82**(A11), 1458–1466 (2004).
Stepanek, F., and Ansari, M. A. *Chem. Eng. Sci.* **60**(14), 4019–4029 (2005).
Stepanek, F., Hanika, J., Marek, M., and Adler, P. M. *Catal. Today* **66**, 249–254 (2001a).
Stepanek, F., Marek, M., and Adler, P. M. *Chem. Eng. Sci.* **56**, 467–474 (2001b).
Stepanek, F., Kubicek, M., Marek, M., and Adler, P. M., Computer-Aided Screening of Adsorbents and Porous Catalyst Carriers, *in* "European Symposium on Computer Aided Process Engineering – 10" (S. Pierucci Ed.), pp. 667–672. Elsevier Science, Amsterdam (2000).
Stepanek, F., Marek, M., and Adler, P. M. *AIChE J.* **45**, 1901–1912 (1999).
Texter, J., and Tirrell, M. *AIChE J.* **47**, 1706–1710 (2001).
Thompson, K. E. *AIChE J.* **48**, 1369–1389 (2002).
Thomson, K. T., and Gubbins, K. E. *Langmuir* **16**, 5761–5773 (2000).
Thornton, C., Ciomocos, M. T., and Adams, M. J. *Powder Technol.* **105**, 74–82 (1999).
Thornton, C., Ciomocos, M. T., and Adams, M. J. *Powder Technol.* **140**, 258–267 (2004).
Thovert, J. -F., Salles, J., and Adler, P. M. *J. Microsc.* **170**, 65–79 (1993).
Thovert, J. -F., Yosefian, F., Spanne, P., Jacquin, G., and Adler, P. M. *Phys. Rev. E* **63**, 061307 (2001).
Tian, Z., Xu, Y., and Lin, L. *Chem. Eng. Sci.* **59**, 1745–1753 (2004).
Torquato, S. *Int. J. Solids Struct.* **37**, 411–422 (2000).
Torquato, S., "Random Heterogeneous Materials: Microstructure and Macroscopic Properties". Sprinder-Verlag, New York (2002).
Torquato, S., Hyun, S., and Donev, A. *Phys. Rev. Lett.* **89**, 266601 (2002).
Tsuji, Y., Kawaguchi, T., and Tanaka, T. *Powder Technol.* **77**, 79–87 (1993).
Tzschichholz, F., Herrmann, H. J., and Zanni, H. *Phys. Rev. E* **53**, 2629–2637 (1996).
van Neer, F., and Bliek, A. *Chem. Eng. Sci.* **54**(20), 4483–4499 (1999).
Velev, O. D., and Lenhoff, A. M. *Curr. Opin. Colloid Interf. Sci.* **5**, 56–63 (2000).
Weyland, M., Midgley, P. A., and Thomas, J. M. *J. Phys. Chem. B* **105**, 7882–7886 (2001).
Whitaker, S., "The Method of Volume Averaging". Kluwer Academic Publishers, Dordrecht (1999).
Wolff, J., Papathanasion, A. G., Rotermund, H. H., Ertl, G., Li, X., and Kevrekidis, I. G. *J. Catal.* **216**(1–2), 246–256 (2003).
Wood, B. D., Quintard, M., and Whitaker, S. *Biotechnol. Bioeng.* **77**, 495–516 (2002a).
Wood, J., Gladden, L. F., and Keil, F. J. *Chem. Eng. Sci.* **57**, 3047–3059 (2002b).
Xia, Y., Gates, B., Tin, Y., and Lu, Y. *Adv. Mater.* **12**, 693–713 (2000).
Xu, H., and Goedel, W. A. *Langmuir* **18**, 2363–2367 (2002).
Xu, Y., and Platzer, B. *Chem. Eng. Technol.* **24**, 773–783 (2001).
Yang, P., Rizvi, A. H., Messer, B., Chmelka, B. F., Whitesides, G. M., and Stucky, G. D. *Adv. Mater.* **13**, 427–431 (2001).
Yao, J., Zhang, Y., Wang, C. -H., Matsusaka, S., and Masuda, H. *Ind. Eng. Chem. Res.* **43**, 7181–7199 (2004).
Yeong, C. L. Y., and Torquato, S. *Phys. Rev. E* **57**, 495–506 (1998a).
Yeong, C. L. Y., and Torquato, S. *Phys. Rev. E* **58**(1), 224–233 (1998b).

Zalc, J. M., Reyes, S. C., and Iglesia, E. *Chem. Eng. Sci.* **58**, 4605–4617 (2003).
Zalc, J. M., Reyes, S. C., and Iglesia, E. *Chem. Eng. Sci.* **59**, 2947–2960 (2004).
Zhdanov, V. P., and Kasemo, B. *Surf. Sci. Rep.* **39**, 25–104 (2000).
Zhdanov, V. P. *Surf. Sci. Rep.* **45**(7–8), 231–326 (2002).